

**An Updated Analysis of Inert Higgs Doublet Model
in light of the Recent Results from
LUX, PLANCK, AMS-02 and LHC**

Abdesslam Arhrib^{1,2}, Yue-Lin Sming Tsai^{2,3}, Qiang Yuan^{4,5} and Tzu-Chiang Yuan²

¹*AbdelMalek Essaadi University, Faculty of Science
and Techniques, B.P 416 Tangier, Morocco*

²*Institute of Physics, Academia Sinica, Nankang, Taipei 11529, Taiwan*

³*Kavli IPMU (WPI), University of Tokyo, Kashiwa, Chiba 277-8583, Japan*

⁴*Key Laboratory of Particle Astrophysics, Institute of High Energy Physics,
Chinese Academy of Sciences, Beijing 100049, P. R. China*

⁵*Key Laboratory of Dark Matter and Space Astronomy, Purple Mountain Observatory,
Chinese Academy of Sciences, Nanjing 210008, P. R. China*

(Dated: October 29, 2018)

Abstract

In light of the recent discovery by the ATLAS and CMS experiments at the Large Hadron Collider (LHC) of a Higgs-like particle with a narrow mass range of 125-126 GeV, we perform an updated analysis on one of the popular scalar dark matter models, the Inert Higgs Doublet Model (IHDM). We take into account in our likelihood analysis of various experimental constraints, including recent relic density measurement, dark matter direct and indirect detection constraints as well as the latest collider constraints on the invisible decay width of the Higgs boson and monojet search at the LHC. It is shown that if the invisible decay of the standard model Higgs boson is open, LHC as well as direct detection experiments like LUX and XENON100 could put stringent limits on the Higgs boson couplings to dark matter. We find that the most favoured parameter space for IHDM corresponds to dark matter with a mass less than 100 GeV or so. In particular, the best-fit points are at the dark matter mass around 70 GeV where the invisible Higgs decay to dark matter is closed. Scalar dark matter in the higher mass range of 0.5-4 TeV is also explored in our study. Projected sensitivities for the future experiments of monojet at LHC-14, XENON1T and AMS-02 one year antiproton flux are shown to put further constraints on the existing parameter space of IHDM.

I. INTRODUCTION

The 7 TeV and 8 TeV run at the Large Hadron Collider (LHC) have revealed and confirmed the existence of a Higgs-like particle h in the standard model (SM) with mass in the narrow range of 125-126 GeV [1, 2]. This discovery is also verified by the recent Tevatron final results [3]. The observation of this new particle combines evidence in the decays $h \rightarrow \gamma\gamma$, $h \rightarrow ZZ^*$ and $h \rightarrow W^\pm W^\mp$. Different signal strengths, defined as the product of Higgs boson production cross sections from different channels and the branching ratios for different decay modes normalized to the corresponding products in SM, have been measured with good precision by both experiments at ATLAS and CMS [4–6]. These measurements will be further improved in the future 13-14 TeV run at the LHC, and perhaps at a future International Linear Collider (ILC) should this machine ever be built. From these signal strengths measurement one can extract information on the couplings of this Higgs-like particle to the gauge bosons and SM fermions. From the most recent measurements, extraction of this Higgs-like particle couplings to SM particles seem to be consistent to a great extent with those of the SM Higgs boson couplings [7]. Moreover, data collected both at ATLAS and CMS indicate that this Higgs-like particle has zero spin and is CP-even, *i.e.* $J^P = 0^+$ is preferred [8, 9].

The discovery of the Higgs-like particle at the LHC indicates for the first time that fundamental scalar exists in Nature. Certainly, many phenomenological models that extend the SM scalar sector with just one scalar doublet existed already in the literature. Some of them are motivated by physics of the dark matter (DM) or neutrinos masses. Among these extensions, we have models with multiple Higgs doublets, with one Higgs doublet and multiple singlets or triplets etc. All these extensions should have one light scalar with Higgs-like couplings to SM particles in the range tolerated by signal strength measurements. Indeed many studies (see for example the references in [7]) have been done using these data to constrain various extensions of the scalar sector of the SM.

In this paper, we concentrate on the Inert Higgs Doublet Model (IHDM) which is a very simple extension of the SM. It was first proposed by Deshpande and Ma [10] in order to study the pattern of electroweak symmetry breaking. The IHDM is an attractive model due to its simplicity. It is basically a Two Higgs Doublet Model (THDM) (see [11] for a recent overview) with an imposed exact \mathbb{Z}_2 symmetry. Under the \mathbb{Z}_2 symmetry, all the SM

particles are even representing the visible sector, while the new Higgs doublet field is odd representing the inert dark sector. Imposing the \mathbb{Z}_2 symmetry forbids the second Higgs doublet developing a vacuum expectation value (VEV) and all the inert particles in this doublet can only appear in pair in their interaction vertices. Indeed, recent studies [12–15] of global fits of the LHC data suggest that the couplings between the W and Z gauge bosons with the new 125-126 GeV Higgs-like boson are very close to their SM values. The new 125-126 GeV boson may play the entire role of electroweak symmetry breaking (EWSB) and leave no room for other Higgs fields to develop any VEVs. This favors the IHDM. As a result, IHDM exhibits very interesting phenomenology. It predicts the existence of a neutral scalar field, denoted generically by χ here, which is the Lightest Odd Particle (LOP) in this model and will play the role of DM candidate. The Higgs mechanism provides a portal for communication between the inert dark sector and the visible SM sector. Thus if kinematics allowed, the SM Higgs boson may decay into a pair of DM χ and will contribute to the invisible SM Higgs boson width which is now constrained by the LHC data. Moreover, annihilation of χ into SM particles will provide thermal relic density and the scattering of χ onto nucleons will lead to direct detection signatures. Therefore, IHDM could be considered as a simple but competitive model in the market with a weakly interacting massive particle (WIMP). As we will see later, IHDM could predict correct DM relic density as well as a cross section for scattering of χ onto nucleons that is consistent with existing data from direct detection. Almost three decades later, IHDM was extended further by Ma [16] to include three \mathbb{Z}_2 odd weak singlets of right-handed neutrinos with Majorana masses. In this extended model [16], a radiative seesaw mechanism for light neutrino masses was proposed and either χ or one of the right-handed neutrinos could be DM candidate. We will not consider this extended version of IHDM in this work but would like to return to this in the future [17].

As mentioned earlier, there have been many attempts to introduce DM Higgs models by extending the SM scalar sector with more singlets or doublets [18–22]. In particular, the phenomenology of IHDM had been extensively discussed in the context of DM phenomenology [23–28] and also for collider phenomenology [29–31]. IHDM has been also advocated to explain the naturalness problem [32]. In the present study, we will reconsider the IHDM model in light of the recent ATLAS and CMS discovery of a Higgs-like particle of 125-126 GeV. We assume that the LOP must fulfill the recent relic density measurement by PLANCK [33].

As a good DM candidate test, we also consider the constraints from DM direct and indirect detection. For the constraint from DM direct detection search, we study the impact from the most recent LUX upper limit [34] which provides a robust constraint on the parameter space. As for indirect detection, we will take into account the Fermi-LAT γ -ray observations of the dwarf spheroidal galaxies (dSphs) [35] and the Galactic center (GC) [36]. In addition to γ -rays, we also include constraints from cosmic ray electrons/positrons from AMS-02 [37], PAMELA [38], and Fermi-LAT [39, 40], and cosmic ray anti-protons from PAMELA [41]. These constraints will be also supplemented by the LHC constraints such as monojet and diphoton signal strength measurement as well as constraint on the Higgs boson invisible decay width.

Some of the above aspects for IHDM have been discussed in recent studies [23, 24]. The compatibility of a heavy SM Higgs boson with LHC results and XENON100 data [42] were discussed in Ref. [23]¹. Similar issues for IHDM were discussed in Ref. [24] with the inclusion of radiative corrections to the scalar masses of the model. Ref. [24] also included renormalization group effects for the quartic scalar couplings λ_i in order to evaluate vacuum stability, perturbativity and unitarity constraints at a higher scale. In our analysis, we will go further by including also the following aspects:

1. Larger parameter space for DM mass: we will scan m_χ from 5 GeV to 4 TeV.
2. LHC monojet constraint in the likelihood.
3. Accurate DM indirect detection likelihood.
4. Constraints from the first result of LUX in direct detection likelihood.
5. Future sensitivity to monojet search at LHC with 14 TeV at the planned luminosity of 100 fb^{-1} and 300 fb^{-1} .
6. Sensitivity to AMS-02 anti-protons and XENON1T.

The layout of this paper is as follows. In section 2, we briefly review IHDM and its parameterization. We then list the theoretical constraints such as perturbativity, perturbative

¹ In a note added in [23], the consistency of IHDM with the 125-126 GeV Higgs-like particle observed at LHC and XENON100 were also discussed.

unitarity and vacuum stability that must be satisfied by the scalar potential parameters. The constraints from collider searches that IHDM is subjected to are discussed in section 3. These include: electroweak precision test constraints, W and Z width constraints, negative search for charginos and neutralinos from LEP-II that could restrict the inert Higgs bosons masses, diphoton signal strength measurement as well as monojet constraint from DM search at LHC. In section 4, we will discuss the relic density measurement by PLANCK as well as DM direct detection and indirect detection constraints. In section 5, we present our methodology for likelihood analysis and explain how all the constraints are included. We present our numerical results in section 6. Future experimental constraints from LHC-14, XENON1T and AMS-02 are discussed in section 7. We conclude in section 8.

II. INERT HIGGS DOUBLET MODEL (IHDM)

In this section, we briefly review the salient features of IHDM and discuss some existing theoretical constraints.

A. Parameterization of the IHDM scalar potential

The IHDM [10] is a rather simple extension of the SM Higgs sector. It contains the SM Higgs doublet H_1 and an additional Higgs doublet H_2 . This model has a \mathbb{Z}_2 symmetry under which all the SM fields including H_1 are even while H_2 is odd under \mathbb{Z}_2 : $H_2 \rightarrow -H_2$. We further assume that \mathbb{Z}_2 symmetry is not spontaneously broken *i.e.* H_2 field does not develop VEV. These doublets can be parameterized as:

$$H_1 = \begin{pmatrix} G^+ \\ \frac{1}{\sqrt{2}}(v + h + iG^0) \end{pmatrix}, \quad H_2 = \begin{pmatrix} H^+ \\ \frac{1}{\sqrt{2}}(S + iA) \end{pmatrix} \quad (1)$$

where G^\pm and G^0 are the charged and neutral Goldstone bosons respectively, which will be absorbed by the W^\pm and Z to acquire their masses.

The scalar potential with an exact \mathbb{Z}_2 symmetry forbids the mass term $-\mu_{12}^2(H_1^\dagger H_2 + \text{h.c.})$ which mixes H_1 and H_2 . Thus it has one fewer term than in THDM, *i.e.*

$$V = \mu_1^2 |H_1|^2 + \mu_2^2 |H_2|^2 + \lambda_1 |H_1|^4 + \lambda_2 |H_2|^4 + \lambda_3 |H_1|^2 |H_2|^2 + \lambda_4 |H_1^\dagger H_2|^2 + \frac{\lambda_5}{2} \left\{ (H_1^\dagger H_2)^2 + \text{h.c.} \right\}. \quad (2)$$

The electroweak gauge symmetry is broken when H_1 doublet gets its VEV: $\langle H_1^T \rangle = (0, v/\sqrt{2})$ while $\langle H_2 \rangle = 0$. This pattern of symmetry breaking ensures unbroken \mathbb{Z}_2 symmetry and results in one more CP-even neutral scalar S , one CP-odd neutral scalar A , a pair of charged scalars H^+ and H^- in addition to the SM CP-even scalar Higgs h . Note that since h is the SM Higgs boson, it is \mathbb{Z}_2 even, while S , A and H^\pm are \mathbb{Z}_2 odd. Moreover, the exact \mathbb{Z}_2 symmetry naturally imposes the flavor conservation. Only SM Higgs boson couples to SM fermions while the inert Higgses S , A and H^\pm do not. The \mathbb{Z}_2 symmetry also ensures the stability of the lightest scalar (S or A) that can act as a DM candidate. DM phenomenology of IHDM had been studied extensively in the literature [23, 24, 26–30, 43].

The above scalar potential in Eq. (2) has 8 real parameters: 5 λ_i , 2 μ_i^2 and the VEV v . Minimization condition for the scalar potential eliminates μ_1^2 in favour of the Higgs mass and the VEV v is fixed to be 246 GeV by the weak gauge boson masses. We are left with 6 independent real parameters. The masses of all the four physical scalars can be written in terms of $\mu_2^2, \lambda_1, \lambda_2, \lambda_3, \lambda_4$ and λ_5 as the following

$$m_h^2 = -2\mu_1^2 = 2\lambda_1 v^2 \quad (3)$$

$$m_S^2 = \mu_2^2 + \frac{1}{2}(\lambda_3 + \lambda_4 + \lambda_5)v^2 = \mu_2^2 + \lambda_L v^2 \quad (4)$$

$$m_A^2 = \mu_2^2 + \frac{1}{2}(\lambda_3 + \lambda_4 - \lambda_5)v^2 = \mu_2^2 + \lambda_A v^2 \quad (5)$$

$$m_{H^\pm}^2 = \mu_2^2 + \frac{1}{2}\lambda_3 v^2 \quad (6)$$

where

$$\lambda_{L,A} = \frac{1}{2}(\lambda_3 + \lambda_4 \pm \lambda_5). \quad (7)$$

Four of the five quartic couplings can be written in terms of physical scalar masses and μ_2^2 as the following expressions

$$\lambda_1 = \frac{m_h^2}{2v^2}, \quad \lambda_3 = \frac{2}{v^2}(m_{H^\pm}^2 - \mu_2^2), \quad (8)$$

$$\lambda_4 = \frac{(m_S^2 + m_A^2 - 2m_{H^\pm}^2)}{v^2}, \quad \lambda_5 = \frac{(m_S^2 - m_A^2)}{v^2}. \quad (9)$$

We are then free to take $(\lambda_i)_{i=1,\dots,5}$ and μ_2^2 as 6 independent parameters, or equivalently, the following set

$$\{m_h, m_S, m_A, m_{H^\pm}, \lambda_2, \lambda_L\} \quad (10)$$

which is more convenient for our purposes to describe the full scalar sector. In our tree level parameterization, λ_A can be expressed as

$$\lambda_A = \lambda_L - \lambda_5 = \lambda_L + \frac{m_A^2 - m_S^2}{v^2}. \quad (11)$$

It is clear from Eq. (11) that $\lambda_A > \lambda_L$ for $m_A > m_S$ and $\lambda_A < \lambda_L$ for $m_A < m_S$. In our systematic scan in the following numerical work, we will consider both cases where $\chi = S$ or $\chi = A$ being the LOP. Thus, the DM mass is defined as

$$m_\chi = \min\{m_S, m_A\}. \quad (12)$$

In order to illustrate constraint on $\lambda_{L,A}$ with S or A being the LOP, we define the coupling $g_{h\chi\chi}$ as

$$g_{h\chi\chi} = -2v\lambda_{\chi\chi} \quad \text{with} \quad \lambda_{\chi\chi} = \begin{cases} \lambda_L & \text{if } \chi = S, \\ \lambda_A & \text{if } \chi = A. \end{cases} \quad (13)$$

The coupling $g_{h\chi\chi}$ shows up directly in the relic density computation depends on whether $\chi = S$ or $\chi = A$.

B. Theoretical constraints

The parameters of the scalar potential of the IHDM are severely constrained by theoretical constraints. First, to trust our perturbative calculations we have to require all quartic couplings in the scalar potential of Eq. (2) to obey $|\lambda_i| \leq 8\pi$. Second, in order to have a scalar potential bounded from below we must also demand the following constraints [11]:

$$\lambda_{1,2} > 0 \quad \text{and} \quad \lambda_3 + \lambda_4 - |\lambda_5| + 2\sqrt{\lambda_1\lambda_2} > 0 \quad \text{and} \quad \lambda_3 + 2\sqrt{\lambda_1\lambda_2} > 0. \quad (14)$$

Third, to further constrain the scalar potential parameters of the IHDM one can impose tree-level unitarity in a variety of scattering processes among the various scalars and gauge bosons. For the unitarity constraints, it is convenience to define the following twelve parameters e_i [27]:

$$e_{1,2} = \lambda_3 \pm \lambda_4 \quad , \quad e_{3,4} = \lambda_3 \pm \lambda_5 \quad , \quad (15)$$

$$e_{5,6} = \lambda_3 + 2\lambda_4 \pm 3\lambda_5 \quad , \quad e_{7,8} = -\lambda_1 - \lambda_2 \pm \sqrt{(\lambda_1 - \lambda_2)^2 + \lambda_4^2} \quad , \quad (16)$$

$$e_{9,10} = -3\lambda_1 - 3\lambda_2 \pm \sqrt{9(\lambda_1 - \lambda_2)^2 + (2\lambda_3 + \lambda_4)^2} \quad , \quad (17)$$

$$e_{11,12} = -\lambda_1 - \lambda_2 \pm \sqrt{(\lambda_1 - \lambda_2)^2 + \lambda_5^2} \quad . \quad (18)$$

The perturbative unitarity constraints are then imposed on all e_i satisfying [27]

$$|e_i| \leq 8\pi, \forall i = 1, \dots, 12. \quad (19)$$

We observe that $e_{9,10}$ give the strongest constraints on $\lambda_{1,2}$ when $2\lambda_3 + \lambda_4 = 0$, which translate into

$$\lambda_{1,2} \leq \frac{4\pi}{3}. \quad (20)$$

In fact, from Eq. (3) with $m_h = 126$ GeV and $v = 246$ GeV we have $\lambda_1 = \frac{m_h^2}{2v^2} = 0.13$ which is well below the unitarity bound given by Eq. (20).

III. COLLIDER CONSTRAINTS

In this section, we discuss DM constraints from the collider search experiments. We will focus on the constraints from the electroweak precision test (EWPT) experiments at LEP-II, neutral and charged Higgs search at LEP-II, as well as the mass and the invisible width of the Higgs, diphoton signal strength and monojet search from the LHC.

- **Electroweak precision tests:**

EWPT is a common approach to constrain physics beyond SM by using the global electroweak fit through the oblique S , T and U parameters [44]. It is well known that in the SM the EWPT implies a close relation between the three masses m_t , m_h and m_W . Similarly, in the IHDM, the EWPT implies constraints on the mass splitting among the Higgs boson masses [32]. In this study, we will use the PDG values of S and T with U fixed to be zero [45]. We allow S and T parameters to be within 95% C.L. (Confidence Level). The central value of S and T , assuming a SM Higgs boson mass of $m_h = 126$ GeV, are given by [45] :

$$S = 0.05 \pm 0.09, \quad T = 0.08 \pm 0.07. \quad (21)$$

The correlation between S and T is 91% in this fit. Analytic expressions for S and T in IHDM can be found in Ref. [32].

- **LEP limits on neutral and charged Higgs bosons:**

Other LEP constraints come from the precise measurements of W and Z widths. In order not to affect these decay widths we demand that the channels $W^\pm \rightarrow \{SH^\pm, AH^\pm\}$

and/or $Z \rightarrow \{SA, H^+H^-\}$ are kinematically not open. This leads to the following constraints: $m_{S,A} + m_{H^\pm} > m_W$, $m_A + m_S > m_Z$ and $2m_{H^\pm} > m_Z$ [46].

Additional constraints on the charged Higgs boson H^\pm , CP-even S and CP-odd A masses can be derived. Note that LEP, Tevatron and LHC bounds on H^\pm and A can not apply because the standard search channels assumes that those scalars decays into a pair of fermions which are absent in the IHDM due to \mathbb{Z}_2 symmetry.

In the IHDM, if S is the LOP the CP-odd A could decay like $A \rightarrow SZ$, while the charged Higgs boson H^\pm could decay into $W^\pm S$ and/or $W^\pm A$ followed by $A \rightarrow SZ$. Therefore the final states of the two production processes $e^+e^- \rightarrow H^+H^-$ and $e^+e^- \rightarrow SA$ would be multi-leptons or multi-jets, depending on the decay products of W^\pm and Z , plus missing energies. To certain extents, the signatures for the charged Higgs case would be similar to the supersymmetry searches for charginos and neutralinos at e^+e^- or at hadron colliders [29, 30].² Taking into account these considerations, we will safely choose in our scan for the charged Higgs mass m_{H^\pm} being always greater than 70 GeV. For the neutral inert Higgses S and A , neutralinos search at LEP-II via $e^+e^- \rightarrow \tilde{\chi}_1^0\tilde{\chi}_2^0$ followed by $\tilde{\chi}_2^0 \rightarrow \tilde{\chi}_1^0 f\bar{f}$ [48] could apply here since the process $e^+e^- \rightarrow SA$ followed by the cascade $A \rightarrow SZ \rightarrow Sf\bar{f}$ would give similar signals. Such analysis had been carefully done in Ref. [31]. Their limits on m_S and m_A can be summarized as $\max(m_A, m_S) \geq 100$ GeV. However, in the present study, we will use the exact exclusion region as given in Ref. [31].

- **Higgs mass:**

In the IHDM, the SM Higgs boson h have similar couplings to SM fermions and gauge bosons. Therefore, as long as h decays into SM final states, all the measurements from ATLAS and CMS experiments about SM Higgs boson properties can be used. In particular, we will require the mass of the SM Higgs boson of the IHDM should lie

² The projection of the experimental limits from SUSY searches to IHDM has to be made with some care since the production cross sections for the fermionic chargino/neutralino pair in the SUSY case are different from the scalar pairs of $H^\pm H^\mp$ and SH^\pm in the IHDM case [47]. The cross sections for fermionic and scalar pair production are scaled by $\beta^{1/2}$ and $\beta^{3/2}$ respectively, where β is the velocity of the final state particle in the center-of-mass frame. Hence, the scalar pair will be suppressed by an extra factor of β as compared with the fermionic case.

within the measurement [6]:

$$m_h = 125.8 \pm 0.6 \text{ (GeV)} . \quad (22)$$

- **Invisible decay:**

The openings of one of the non-standard decays of the Higgs boson such as $h \rightarrow SS$ or $h \rightarrow AA$ ³, hence $h \rightarrow H^+H^-$ is not open. can modify the total width of the Higgs boson and can have significant impact on LHC results. Since either $\chi = S$ or A is the lightest \mathbb{Z}_2 odd particle, it will be stable and the decay $h \rightarrow \chi\chi$ will be invisible. Both ATLAS and CMS had performed searches for invisible decay of the Higgs boson [49–51]. Using the Higgs-strahlung SM cross section for $pp \rightarrow ZH$ with a 125 GeV SM Higgs boson, ATLAS [49] has excluded an invisible branching ratio of the Higgs boson larger than 65% with 95% C.L.. CMS also studied the invisible decay of the Higgs boson produced via the vector boson fusion (VBF) mechanism and obtained an upper limit for the invisible branching ratio of 69% with 95% C.L.. When the two production mechanisms are combined the upper limit becomes 54% with 95% C.L. [51]. This constraint on the invisible decay is rather weak compared to the one derived from various works of global fits to ATLAS and CMS data [12–15]. These global fits studies suggest that the branching ratio of the invisible decay of the Higgs boson should not exceed 19% at 95% C.L. in the case where the Higgs boson has SM-like couplings to all SM particles plus additional invisible decay mode which is exactly the case as in IHDM. On the other hand, if one allows for deviation in the $h\gamma\gamma$ (and hgg as well on general grounds but not for IHDM) coupling from its SM value the 95% C.L. limit on the invisible Higgs decay branching ratio moves up to 29% [14].

- **Diphoton signal strength $R_{\gamma\gamma}$ in the IHDM:**

Assuming that the production cross section of the Higgs boson is dominated by the gluon gluon fusion process, the diphoton signal strength in the IHDM normalized to

³ From our previous discussion of LEP-II constraints, we assume $m_{H^\pm} > 70$ GeV in our numerical scan

the SM value can be simplified as

$$\begin{aligned}
R_{\gamma\gamma} &\equiv \frac{\sigma_h^{\gamma\gamma}}{\sigma_{h\text{SM}}^{\gamma\gamma}} = \frac{\sigma(gg \rightarrow h) \times \text{BR}(h \rightarrow \gamma\gamma)}{\sigma(gg \rightarrow h)^{\text{SM}} \times \text{BR}(h \rightarrow \gamma\gamma)^{\text{SM}}} , \\
&= \frac{\text{BR}(h \rightarrow \gamma\gamma)^{\text{IHDM}}}{\text{BR}(h \rightarrow \gamma\gamma)^{\text{SM}}} ,
\end{aligned}
\tag{23}$$

where in the first line we have used the narrow width approximation and in the second line we used the fact that $\sigma(gg \rightarrow h)$ is the same in both the SM and IHDM. Thus the signal strength $R_{\gamma\gamma}$ in IHDM is simply given by the ratio of the branching ratios, which is not necessarily one since the charged Higgs boson in IHDM can provide extra contribution other than the SM particles to the triangle loop amplitude of $h \rightarrow \gamma\gamma$.

At ATLAS, the overall signal strength for diphoton is about $1.55_{-0.28}^{+0.33}$, which corresponds to about 2σ deviation from the SM prediction [52], while the other channels are consistent with SM. However, at CMS, the new analysis for diphoton mode based on multivariate analysis [53] gives a signal strength about 0.78 ± 0.28 , which is consistent with SM. Many proposals based on physics beyond SM, including IHDM, have been suggested to explain the diphoton excess, but the actual disagreement between ATLAS and CMS does not allow to draw any definite conclusions yet, given the current level of statistics. In the present analysis we will not try to explain the diphoton excess but rather study the impact of the other constraints on the ratio $R_{\gamma\gamma}$.

• **LHC monojet search:**

Besides using the invisible width of the Higgs decay, another strategy to look for DM at the LHC is to study high p_T monojet balanced by a large missing transverse energy E_T [54, 55]. Such kind of signature is possible in IHDM by producing the SM Higgs boson h in association with an energetic jet followed by the invisible decay of h . In our analysis we will consider the following parton processes:

- $gb \rightarrow hb \rightarrow \chi\chi + b$: s -channel and t -channel tree level diagrams with the Higgs boson radiated from b quark legs,
- $qg \rightarrow hq \rightarrow \chi\chi + q$: t -channel diagram through tree level gluon-quark-anti-quark vertex and one-loop hgg effective vertex,
- $gg \rightarrow hg \rightarrow \chi\chi + g$: t -channel diagram through tree level three gluon vertex and one-loop hgg effective vertex,

- $q\bar{q} \rightarrow hg \rightarrow \chi\chi + g$: s -channel diagram through tree level gluon-quark-anti-quark vertex and one-loop hgg effective vertex.

In all these processes, the final state consists of a pair of invisible DM particles plus a quark or gluon jet. For the experimental cuts, see the later discussion of the likelihood function for the monojet data in section V.

IV. RELIC DENSITY, DIRECT DETECTION AND INDIRECT DETECTION CONSTRAINTS

It is well known that annihilation of χ into SM particles and other inert Higgs bosons can contribute to thermal relic density as well as indirect DM signals of high energy gamma-rays, positrons, antiprotons or neutrinos, while the scattering of χ onto nuclei will lead to direct detection signals by measuring the recoil energy of the nuclei via scintillation light, heat or ionization or some combinations of these three different signals using different technologies.

- **Relic density constraint:**

Assuming a standard thermal evolution of our Universe, we compute the relic density from the following channels: $\chi\chi \rightarrow f\bar{f}$ ($f = t, b, c, \tau, \mu$), $\chi\chi \rightarrow W^\pm W^\mp, ZZ, \gamma\gamma, \gamma Z$ and $\chi\chi \rightarrow H^\pm H^\mp$. Since χ can be either S or A , we consider SS or AA annihilation. Note that in the case where $m_\chi < m_{W,Z}$, we take into account the annihilation into 3-body final state from VV^* or 4-body final state from V^*V^* ($V = W^\pm, Z$). All the annihilation into SM particles channels proceed through s -channel Higgs boson exchange while the annihilation into inert Higgs particles such as $H^\pm H^\mp$, hh and AA will proceed through both s -channel and t -channel Higgs boson exchange as well as the contact interactions with the quartic couplings for the $\chi\chi H^\pm H^\mp$, $\chi\chi hh$ and $\chi\chi AA/SS$ vertices. The calculation is done using the public code `MicrOMEGAs` [56]. The outcome of our relic density calculation should be in agreement with the recent PLANCK measurement [57]:

$$\Omega_{\text{CDM}} h^2 = 0.1199 \pm 0.0027 . \quad (24)$$

As is well known if the mass splitting between the LOP and Next-Lightest Odd Particle (NLOP) is $\lesssim 10$ GeV or so, the number densities of these NLOPs have only slight

Boltzmann suppression with respect to the LOP number density. Therefore, the contributions to the relic density from the scattering of LOP-NLOP and NLOP-NLOP have to be taken into account in order to have a more precise relic density prediction. These mechanisms are known as coannihilation [58, 59]. As these are implemented already in the package `MicrOMEGAs` [56], we can take the $S - A$, $S - H^\pm$ and $A - H^\pm$ coannihilation into account at ease.

- **The LUX limit:**

At present the most stringent limit on the spin-independent component of elastic scattering cross section σ_p^{SI} for $\chi p \rightarrow \chi p$ comes from LUX [34]. They improved the minimum σ_p^{SI} upper limit obtained by XENON100 [42] about an overall factor of 3. This result then sets the limit on the spin-independent cross section, $\sigma_p^{\text{SI}} < 8 \times 10^{-10}$ pb for DM mass $m_\chi \approx 33$ GeV. In this study, we include the 90% upper limit obtained in [34] for σ_p^{SI} versus the DM mass in our likelihood function. However, one should bear in mind that σ_p^{SI} may be susceptible to large theoretical uncertainties from the hadronic matrix elements. We will take into account the uncertainties in the hadronic matrix elements, as will be discussed later in section V.

- **Gamma-rays:**

We consider the Fermi-LAT observations of γ -rays from dSphs [35, 60, 61] and GC [36]. The 10 dSphs as adopted in [35] will be used in this work. Four years of the Fermi-LAT data ⁴, recorded from 4 August 2008 to 2 August 2012 with the pass 7 photon selection, are employed in this analysis. The energy range of photons is chosen from 200 MeV to 500 GeV, and the region-of-interest (ROI) is adopted to be a $14^\circ \times 14^\circ$ box centered on each dSphs. For the GC analysis, a slightly smaller ROI region of $10^\circ \times 10^\circ$ is chosen to avoid too many sources in the analysis. In the likelihood analysis, the normalization of the diffuse background models ⁵ `gal_2yearp7v6_v0.fits` and `iso_p7v6source.txt`, and the point sources located in the ROIs in the second LAT catalog [62] are left free to do the minimization. The Fermi-LAT data are binned into 11 energy bins logarithmically spaced between 0.2 and 410 GeV, and we calculate

⁴ <http://fermi.gsfc.nasa.gov/ssc/data>

⁵ <http://fermi.gsfc.nasa.gov/ssc/data/access/lat/BackgroundModels.html>

the likelihood map of Fermi-LAT dSphs and GC observations on the E_{bin} –flux plane following the method developed in [61]. Such a method is very efficient to derive the final likelihood of any specific γ -ray spectrum, and is tested to be consistent with the standard analysis procedure using Fermi Scientific Tool [61].

- **Cosmic ray electrons and positrons:**

The cosmic ray positron fraction measured by PAMELA [38] and most recently by AMS-02 [37] show clear evidence of excess compared with the secondary production as expected from the cosmic ray propagation model. The fluxes of the total e^+e^- measured by ATIC [63], Fermi-LAT [40], HESS [64] and MAGIC [65] also show the deviation from the extrapolation of the low energy PAMELA data [66], which further supports the existence of extra e^+e^- sources. There are many models proposed to account for the e^+e^- excesses, including the astrophysical sources such as pulsars and supernova remnants, and DM annihilation/decay (see *e.g.* the review articles [67]).

While the DM model would suffer from strong constraints from γ -ray observations [68], it has been shown that the pulsars with reasonable parameters can explain the positron fraction as well as the electron plus positron flux data [69]. Therefore in this work we first fit both data set with the background plus pulsar-like models, and then add the DM contributions from IHDM to calculate their likelihoods [70]. The framework for doing such calculation in this astrophysical setting can be found in [71]. Basically, a Markov Chain Monte Carlo (MCMC) based global fitting tool was used to determine the model parameters. The observational data used in the fit include the AMS-02 positron fraction [37], PAMELA electron spectrum [66], and the total e^+e^- spectra of Fermi-LAT [40] and HESS [64]. Note that for the background electron spectrum we employ a three-piece broken power-law function in order to fit simultaneously the above data [71].

The solar modulation affects the fluxes of the particles at low energy. In this work we simply adopt the force-field approximation to account for the solar modulation effect [72]. It was found that the modulation potential $\Phi \approx 970$ MV can fit both the positron fraction and electron spectra. However, for the cosmic ray protons, a smaller modulation potential $\Phi \approx 500$ MV is favoured by the PAMELA data [71, 73]. We leave this as an open question because the solar modulation may indeed depend on

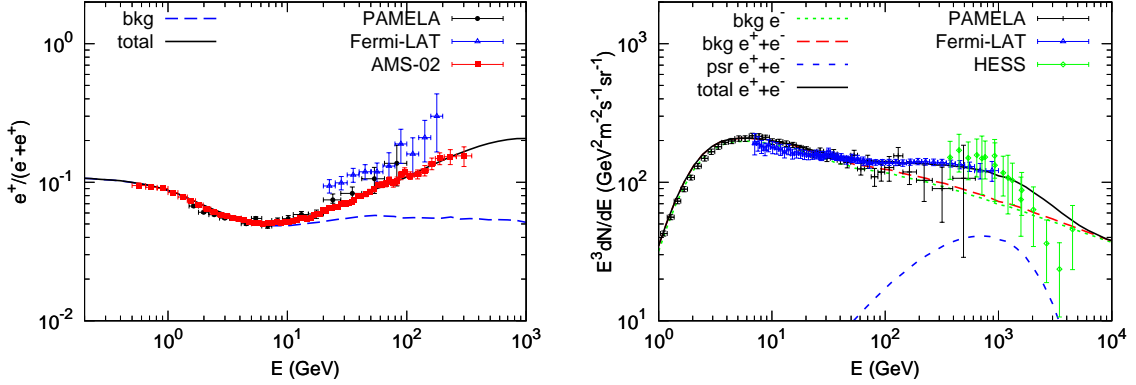


FIG. 1: The positron fraction (*left*) and electron spectra (*right*) for the background + pulsar model. Also shown are the positron fraction data from AMS-02 [37], PAMELA [38] and Fermi-LAT [39], and electron flux data from Fermi-LAT [40], HESS [64] and PAMELA [66].

the mass-to-charge ratio of particles. The best-fitting positron fraction and electron spectra compared with the observational data are shown in Fig. 1. The model fits the data well and the reduced χ^2 is about 0.92.

When calculating the likelihood after adding the DM contributions in IHDM, we further multiply a factor of $\alpha_i E^{\beta_i}$ to the fluxes of the background components ($i = 1, 2, 3$ for the e^- background, e^+ background and pulsar e^\pm respectively), in order to take the uncertainties of the modelling into account [74]. The parameters α_i and β_i are left free and treated as nuisance parameters in our analysis. They are allowed to vary in the range of $0.1 < \alpha_i < 10$ and $-0.5 < \beta_i < 0.5$ to calculate the maximum likelihood of a specific DM model point.

- **Cosmic ray antiprotons:**

The precise measurement of the antiproton-to-proton ratio and antiproton flux by PAMELA show relatively good agreement with the cosmic ray background model expectation [41, 75], which leaves limited space for the DM models [76]. We calculate the expected antiproton flux in the same propagation model used to explain the e^+e^- data, as shown in Fig. 2. The solar modulation potential is adopted to be 500 MV as suggested by PAMELA [71, 73]. Same as the α_i and β_i in e^+e^- case, an adjustment factor $\alpha_{\bar{p}} E^{\beta_{\bar{p}}}$ with nuisance parameters $\alpha_{\bar{p}}$ and $\beta_{\bar{p}}$ varied in the same respective range is employed to account for the uncertainties of the background estimation.

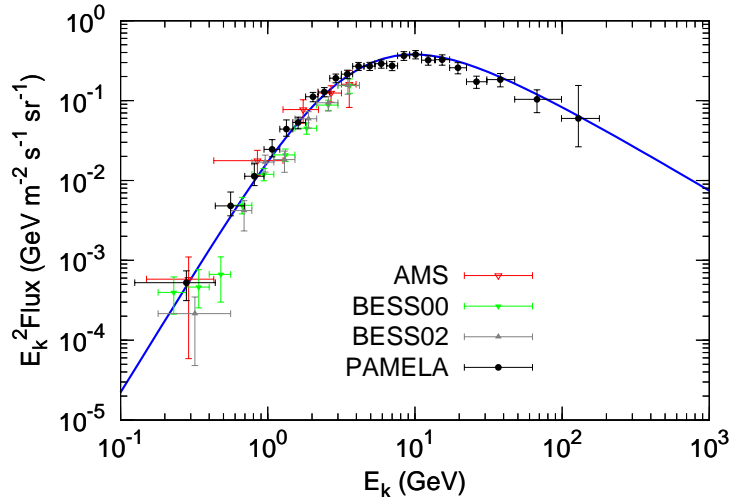


FIG. 2: Antiproton flux of the background model compared with the observational data of AMS [77], BESS00 [78], BESS02 [79] and PAMELA [41].

In Table I, we summarize all the experimental constraints mentioned in this and previous section. To avoid words cluttering in later presentation, we denote the first block of relic density and collider constraints together with the theoretical constraints as **RC** (Relic density and Collider), the second block of LUX constraint as **DD** (Direct Detection) and the third block of constraints as **ID** (Indirect Detection). Additionally, we reject those points during our parameter scans which violate any one of the theoretical constraints on IHDM mentioned in section II B. We note that the data in the **RC** block does not involve large theoretical uncertainties compared with the other two blocks, so we will take special care of this block by including it only at the scan level.

V. METHODOLOGY

In this section, we will describe the statistical treatment of all the experimental constraints discussed in previous two sections and the numerical method used in our analysis. At the fitting level, we use the following different likelihood distributions: Gaussian, Poisson, and error function, depending on which experiments as shown in the fourth column in Table I. For experiments that may lead to 5σ discoveries, it is customary to use Gaussian distribution if experimentalists can provide central values and errors. For counting experiments, Poisson distribution is a standard formula for the likelihood. However, for experimental data like

Measurement	Mean	Error: Exp., Th.	Distribution	Refs.
m_h (by CMS)	125.8 GeV	0.6 GeV, 0.0 GeV	Gaussian	[6]
Ωh^2	0.1199	0.0027, 10%	Gaussian	[33]
S	0.05	0.09, 0.0	Gaussian	[45]
T	0.08	0.07, 0.0	Gaussian	[45]
BR($h \rightarrow$ invisible) (by ATLAS)	0.65	5%, 10%	Error fn.	[49]
$R_{\gamma\gamma}$	0.78	0.28, 20%	Gaussian	[53]
Monojet (by CMS 19.5 fb $^{-1}$)	See text.	See text.	Poisson	[54]
LUX (2013)	See text.	See text.	Error fn.	[34]
dSphs γ -ray	See text.	See text.	Poisson	[35, 61]
GC γ -ray flux	See text.	See text.	Half Poisson	[36]
e^+ fraction, $e^+ + e^-$ flux	See text.	See text.	Gaussian	[37, 38, 40]
\bar{p} flux	See text.	See text.	Gaussian	[41]

TABLE I: The experimental constraints that we include in our likelihood functions to constrain the IHDM model. We denote the first block of relic density and collider constraints together with the theoretical constraints as **RC** (Relic and Collider) , LUX constraint as **DD** (Direct Detection) and the last block of constraints as **ID** (Indirect Detection).

LUX and invisible Higgs decay width where only upper limits are provided, it is difficult to implement Poisson likelihood in the analysis. Under these circumstances, we will follow the procedure described in [80, 81], where the error function was used to smear the experimental bounds.

- **Gaussian likelihood distribution:**

The Gaussian likelihood distribution is related to the χ^2 as

$$\mathcal{L}_{\text{Gaussian}} = e^{-\frac{\chi^2}{2}}, \quad (25)$$

with the χ^2 defined as usual

$$\chi^2 = \frac{(\text{prediction} - \text{experimental central value})^2}{\sigma^2 + \tau^2}, \quad (26)$$

where σ is an experimental error and τ is a theoretical uncertainty. We assume that the theoretical uncertainty τ owes to either the discrepancy between computations using

different methods or unknown high order corrections or non-perturbative uncertainties. See Table I for the list of experiments that we use the Gaussian likelihood distribution.

- **Poisson likelihood distribution:**

Regarding the LHC monojet, we use a Poisson likelihood distribution augmented with an extra Gaussian distribution to account for the background uncertainties. The probability distribution for each p_T^{miss} threshold is then written as

$$\mathcal{P}(s_i + b_i | o_i) = \max_{b'} \left\{ \frac{e^{-(s_i + b')} (s_i + b')^{o_i}}{o_i!} \exp \left[-\frac{(b' - b_i)^2}{2\delta b_i^2} \right] \right\}, \quad (27)$$

where i refers different missing transverse energy \cancel{E}_T cuts described in [54]. We also use the values of background events b with error δb and observed events o from Ref. [54]. To simulate signal events s , we use `MadGraph 5` [82] to compute the cross section at the parton level and apply the appropriate cuts. Following the CMS study [54], we will use the following basic selection requirements for the transverse momentum (p_T^j) and pseudo-rapidity (η^j) of the monojet:

- at least one jet with $p_T^j > 110$ GeV and $|\eta^j| < 2.4$,
- at most two jets with $p_T^j > 30$ GeV,
- and no isolated leptons in the final state.

CMS collaboration [54] also gave the events for seven different cuts on the missing transverse energy \cancel{E}_T between 250 and 550 GeV (in step of 50 GeV), which are largely dominated by the SM (Z, W^\pm) background where Z decays to neutrinos and W^\pm decays leptonically without reconstruction of the charged lepton. For a given \cancel{E}_T threshold, the signal event s_i is the total number of monojet which is given by the monojet cross section after cuts times the CMS luminosity of 19.5 fb^{-1} . Therefore, our likelihood function for CMS monojet search can be written as

$$\mathcal{L}_{\text{LHC-monojet}} = \prod_i \mathcal{P}(s_i + b_i | o_i), \quad (28)$$

where i runs over all the seven different cuts on $\cancel{E}_T(\text{GeV}) > 250, 300, 350, 400, 450, 500$ and 550 [54]. We have tested that using the above likelihood function, we can reproduce the exclusion limits for the effective DM operators analyzed by the CMS [54]. This justifies the use of this likelihood function for the IHDM.

While we also use the normal Poisson distribution to be the likelihood function for the γ -ray from dSphs, a half Poisson distribution is used for the γ -ray from GC. In other words, if the signal events are less than the number of events required for the maximum likelihood, we set its likelihood to be the maximum likelihood. This is because a normal Poisson likelihood of γ -ray from GC would give a very significant signal at $m_\chi \sim$ a few GeV [83]. Since the GC is a very complicated astrophysical environment, it is not clear whether such an excess is due to some kinds of astrophysical background or genuine DM signals. In order to be less biased, we therefore adopt a half Poisson distribution for our GC γ -ray likelihood. Moreover, the halo profiles in GC can also lead to big uncertainties. In this study, we use the isothermal halo profile in order to achieve a more conservative limit.

- **Error function:**

Instead of using a step function, we employ an error function (erfc) likelihood with a theoretical error $\tau = 10\%$ to smear the upper bound on the branching ratio of the invisible Higgs decay width $\text{BR}(h \rightarrow \text{invisible})$,

$$\mathcal{L}_{\text{BR}(h \rightarrow \text{invisible})} = \frac{1}{2} \text{erfc} \left(\frac{\text{prediction} - \text{experimental upper limit}}{\sqrt{2}\tau} \right). \quad (29)$$

For the upper limit of LUX for the χ -nucleon cross section σ_p^{SI} versus the DM mass, we set $\tau = 150\%$ for the hadronic uncertainties to account for the difference between the default value used in `MicrOMEGAs` and 1σ lower limit of the pion-nucleon sigma term $\sigma_{\pi N}$ obtained from lattice calculation [84].

With the above set up of the likelihood distributions for each experiment, we are able to guide our random scan of the parameter space to explore regions with high likelihood probability. The total likelihood is the product of all the individual likelihood from each experiment. As noted earlier, since **DD** and **ID** experimental constraints could suffer from large theoretical uncertainties (*e.g.* in the hadronic matrix elements in **DD** and DM halo profiles in **ID**), we rather play safe and conservative by including only the first **RC** block in Table I in the likelihood at the scan level.

Engaging with `MultiNest v2.18` [85] of 20000 living points, a stop tolerance factor of 10^{-4} , and an enlargement factor reduction parameter of 0.8, we perform 6 random scans in

the six dimensional parameter space which will be restricted in the following ranges for the masses

$$\begin{aligned}
122.0 &\leq m_h / \text{GeV} \leq 129.0 , \\
5.0 &\leq m_S / \text{GeV} \leq 4 \times 10^3 , \\
5.0 &\leq m_A / \text{GeV} \leq 4 \times 10^3 , \\
70.0 &\leq m_{H^\pm} / \text{GeV} \leq 4 \times 10^3 ,
\end{aligned}$$

and the following ranges for the couplings

$$\begin{aligned}
-2.0 &\leq \lambda_L \leq 2.0 , \\
0.0 &\leq \lambda_2 \leq 4.2 .
\end{aligned}$$

Of the total 6 random scans, 3 of them we use flat priors for all the above six parameters, while for the rest of the scans, we use flat priors for m_h and λ_L and log priors for the other four parameters. We note that coverage of the parameter space is the most important aspect for profile likelihood method. We combine these 6 different scans to perform our analysis in order to achieve better coverage of the parameter space and obtain accurate best-fit points. In order to scan the parameter space more efficiently, we set the range of λ_2 up to 4.2 allowed by the unitarity constraint of Eq. (20). We finally collect $\sim 1.2 \times 10^6$ points in these scans.

In the next two sections, we will present our results mainly based on ‘‘Profile Likelihood’’ method [86]. Under the assumption that all uncertainties follow the approximate Gaussian distributions, confidence intervals are calculated from the tabulated values of $\delta\chi^2 \equiv -2\ln(\mathcal{L}/\mathcal{L}_{\max})$. Thus, for a two dimension plot, the 95% confidence (2σ) region is defined by $\delta\chi^2 \leq 5.99$.

We note that the best-fit points in either log or flat prior scan can have almost the same \mathcal{L}_{\max} of individual scan but the locations of m_S and m_A are quite different from these 6 scans. This is due to the fact that we allow the LOP m_χ to be either m_S or m_A . Same value of m_χ corresponds to two positions in m_S for LOP is S or not. Similar situation is found for $m_\chi = m_A$ depending on whether LOP is A or not. However, for the projection to m_χ , the best-fits locate at the same region.

VI. RESULTS AND DISCUSSIONS

A. Low dark matter mass scenario

In this subsection, we will discuss the low DM mass scenario where the invisible Higgs boson decay is open either by $h \rightarrow SS$ or $h \rightarrow AA$ and study the implication from the LHC constraint on such invisible Higgs boson decay as well as LUX and relic density constraints on the $h\chi\chi$ coupling.

Let us first give the analytical expression of the invisible Higgs boson decay branching ratio

$$\text{BR}(h \rightarrow \text{invisible}) = \frac{\Gamma(h \rightarrow \chi\chi)}{\Gamma_{\text{tot}}(h)} = \frac{\Gamma(h \rightarrow \chi\chi)}{\Gamma_{\text{SM}}(h) + \Gamma(h \rightarrow \chi\chi)}, \quad (30)$$

where $\Gamma_{\text{SM}}(h)$ is the total width of the SM Higgs boson taken as $\Gamma_{\text{SM}}(h) = 4.02$ MeV in what follows, and

$$\Gamma(h \rightarrow \chi\chi) = \frac{g_{h\chi\chi}^2}{32\pi m_h} \sqrt{1 - \frac{4m_\chi^2}{m_h^2}}, \quad (31)$$

with $g_{h\chi\chi}$ given by Eq. (13).

In order to understand the correlation between the coupling $g_{h\chi\chi} \propto \lambda_{L,A}$ and the invisible Higgs boson decay branching ratio, we illustrate in Fig. 3 (left) a contour plot for the $\text{BR}(h \rightarrow \text{invisible})$ in the $(m_\chi, |\lambda_{L,A}|)$ plane. The contour lines are, from top to bottom, 65%, 30%, 20% and 10%. The domain bounded by the red curve is the 3σ region allowed by PLANCK measurement of the relic density given by Eq. (24). It is clear that for $|\lambda_{L,A}| \approx 10^{-2}$, one can have an invisible decay branching ratio of the order of 20% for $m_\chi \leq 55$ GeV. As one can see from the region inside the red curve, 10% to 20% invisible Higgs boson decay is consistent with the relic density measurement only for m_χ in the range of 50-56 GeV. This is due to the fact that near the s -channel resonance of the Higgs boson where $m_h \approx 2m_\chi$ the relic density can be significantly enhanced. It is clear that the smaller the invisible Higgs boson decay branching ratio is, the smaller the size of $|\lambda_{L,A}|$ unless the DM mass is close to the threshold region $m_h \approx 2m_\chi$ where $|\lambda_{L,A}|$ could take larger values.

In fact, it is plausible to relate $\text{BR}(h \rightarrow \text{invisible})$ to the spin-independent cross section σ_p^{SI} for direct detection. In the IHDM, the diagram contributed to σ_p^{SI} is given by the t -channel Higgs boson exchange and so it is proportional to $g_{h\chi\chi}^2$ [87]. From the expression of $\text{BR}(h \rightarrow \text{invisible})$ one can then eliminate the $g_{h\chi\chi}^2$ coupling in favour of σ_p^{SI} and other

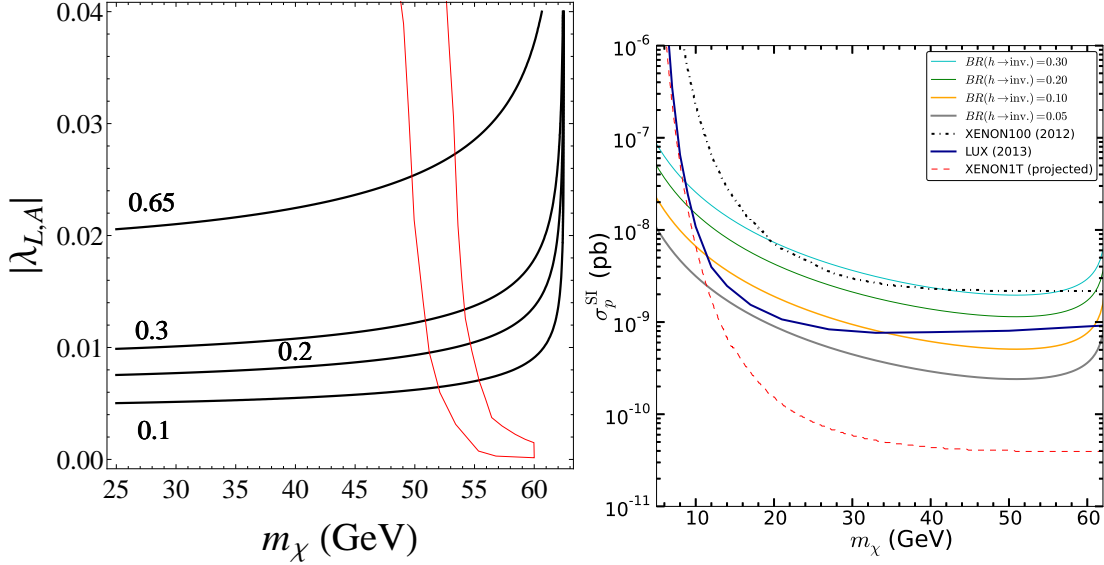


FIG. 3: (*Left*) Contour plots for the invisible Higgs boson decay branching ratio as a function of $|\lambda_{L,A}|$ and $m_\chi = m_{S,A}$. The contours are, from top to bottom, 65%, 30%, 20% and 10%, while the red curve is the 3σ region allowed by PLANCK relic density value. (*Right*) Spin-independent cross section σ_p^{SI} as a function of the DM mass m_χ in IHDM with fixed values of invisible Higgs decay branching ratio, 30%, 20%, 10% and 5% from top to bottom. In both plots we take $m_h = 125$ GeV.

parameters such as the DM mass m_χ , nucleon mass m_N , Higgs mass m_h , form factor f_N , Higgs total width $\Gamma_{\text{SM}}(h)$, and the Higgs VEV v , *viz.*,

$$\text{BR}(h \rightarrow \text{invisible}) = \frac{\sigma_p^{\text{SI}}}{\sigma_p^{\text{SI}} + f(m_N, m_\chi, m_h, f_N)}, \quad (32)$$

where

$$f(m_N, m_\chi, m_h, f_N) = \frac{8\Gamma_{\text{SM}}(h)m_N^2 f_N^2}{m_h^3 v^2 (m_\chi + m_N)^2 \sqrt{1 - \frac{4m_\chi^2}{m_h^2}}}. \quad (33)$$

For a given $f(m_N, m_\chi, m_h, f_N)$ and $\text{BR}(h \rightarrow \text{invisible})$, one can then calculate σ_p^{SI} (see [88] for a similar discussion in the framework of portal models).

We illustrate in Fig. 3 (right) a contour plot for $\text{BR}(h \rightarrow \text{invisible})$ in the plane $(m_\chi, \sigma_p^{\text{SI}})$ where we have used $f_N = 260$ MeV which is roughly the default value used in MicrOMEGAs. We show contour lines for $\text{BR}(h \rightarrow \text{invisible}) = 30\%$, 20% , 10% and 5% . Also shown is the actual limit from XENON100 and LUX as well as the projections from XENON1T experiments. It is remarkable from this plot that $\text{BR}(h \rightarrow \text{invisible}) > 30\%$ is excluded by

XENON100 if m_χ is in the range of 20-60 GeV, while m_χ in the range of 12-32 GeV with $\text{BR}(h \rightarrow \text{invisible}) > 10\%$ is now excluded by LUX. Combining these two plots of Fig. 3, we can conclude that $|\lambda_{L,A}|$ should be less than about 2×10^{-2} for the three experimental constraints of Higgs invisible width from LHC, LUX limit on σ_p^{SI} and relic density from PLANCK to be consistent with each other. Future sensitivity of the XENON1T experiment would be able to exclude invisible Higgs decay branching ratio as low as 1% or less, which can further constrain the couplings $\lambda_{L,A}$ that control the communication between the inert and visible sectors.

B. Current experimental constraints and best-fit result

1. RC

We will use the next three figures to discuss the two dimension profile likelihoods from the **RC** block.

A: Fig. 4

First, in Fig. 4, we present the two dimension profile likelihood on the (m_S, m_A) plane (left) and $(m_{\text{LOP}}, m_{H^\pm})$ plane (right). The contours correspond to the 95% C.L. of **RC** constraints. For the area above the red-dashed line, S is the LOP; while below the red-dashed line, A is the LOP. Generally speaking, the relic density is a strong constraint, since we treat it as a positive measurement with a very small experimental uncertainty rather than an upper limit. For all the parameter space, we found that the DM relic abundance $\Omega_\chi h^2$ is mostly too large, namely, its annihilation in the early Universe is too inefficient. Certain mechanisms, whether they are natural or not, have to play some peculiar roles to enhance the annihilation cross sections so as to reduce the relic abundance. These mechanisms can be clearly identified by the several different branches in the left panel of Fig. 4:

- (1) $m_A \approx m_S$ ($A - S$ coannihilation),
- (2) $2m_\chi \approx m_h$ (the SM Higgs boson resonance), and
- (3) two small branches at $50 \text{ GeV} < m_A, m_S < 70 \text{ GeV}$ (mixed $A - S$ coannihilation and the SM Higgs boson resonance).

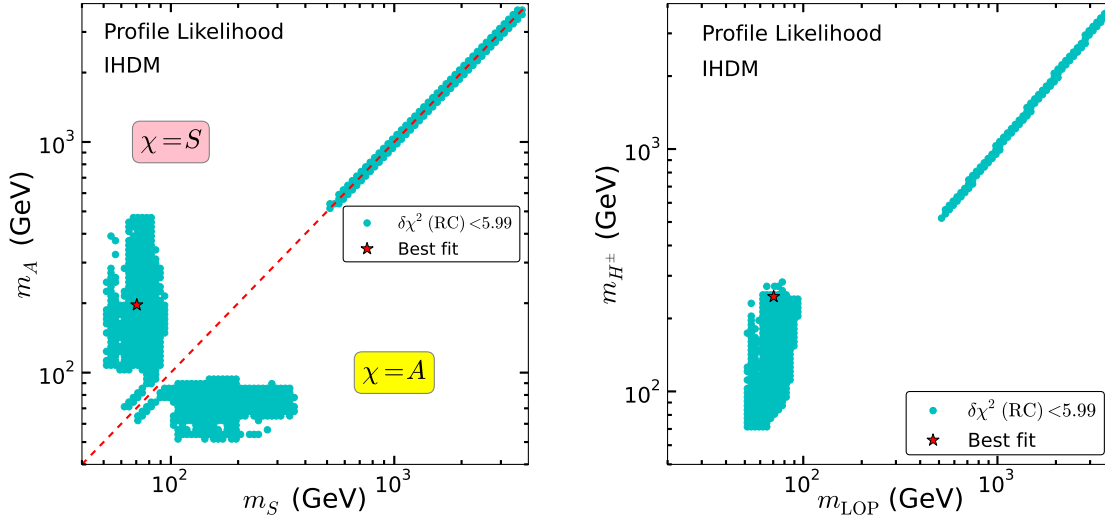


FIG. 4: The two dimension profile likelihood on the (m_S, m_A) plane (*left*) and $(m_{\text{LOP}}, m_{H^\pm})$ plane (*right*). The cyan dots are 95% C.L. (2σ). The best-fit points are marked as the red stars in the plots.

However, inefficient annihilation is not the case at $100 \text{ GeV} < m_\chi < 500 \text{ GeV}$ which has actually too little relic density (see also Fig. 6 of [24]). In fact, this is because the W^+W^- final state is open so that the annihilation cross section can be dramatically enhanced. On the other hand, as the DM mass increases further, the s -channel propagator will give rise to suppression in the cross section that can offset the enhancement from the opening of the W^+W^- in the final state. Thus, a correct DM relic density can be achieved again for $m_\chi > 500 \text{ GeV}$ as indicated by the cyan dots along the diagonal lines in Fig. 4.

In the right panel of Fig. 4, we can see that the charged Higgs boson coannihilation at $m_\chi > 600 \text{ GeV}$ and a nearly box-shaped region of smaller masses in the $(m_{\text{LOP}}, m_{H^\pm})$ plane. We found that in this nearly box-shaped region, the EWPT T constraint will require the mass splitting $m_{H^\pm} - m_A \leq 250 \text{ GeV}$ in the 3σ region. However, there is another limit $m_A - m_{H^\pm} \leq 400 \text{ GeV}$ resulting from $\lambda_A < 4$ (see later for further discussion of the λ_A limit shown in the upper right panel of Fig. 5). In addition, we impose the condition $m_A + m_S > m_Z$ in order to escape the precise measurement of the Z^0 decay width from LEP as well as the search for neutralinos at LEP adapted

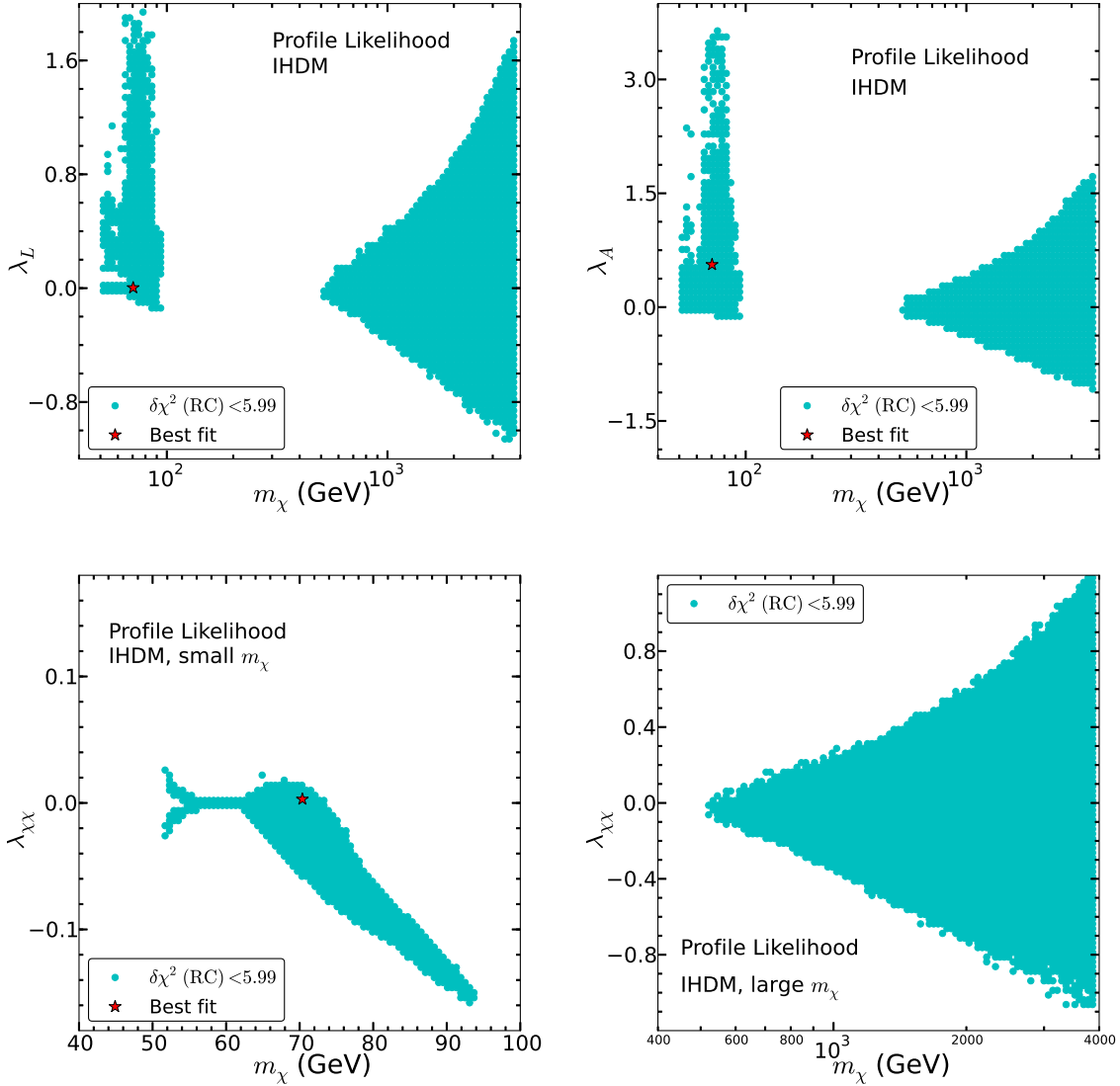


FIG. 5: *Upper plots:* The two dimension profile likelihood on the (m_χ, λ_L) plane (*left*) and the (m_χ, λ_A) plane (*right*). *Lower plots:* The two dimension profile likelihood on the $(m_\chi, \lambda_{\chi\chi})$ plane with low $m_\chi \leq 110$ GeV (*left*) and large $m_\chi \geq 500$ GeV (*right*). The cyan dots are 95% C.L. (2σ). The best-fit points are marked as the red stars in the plots.

here to the IHDM process $e^+e^- \rightarrow SA$ as was done in [31].

B: Fig. 5

Next, we discuss the limits on the two couplings λ_L and λ_A which play the role connecting the inert sector with the visible SM sector. In the upper left and upper right panels of Fig. 5, we show the 95% confidence level region (cyan dots) with the **RC**

constraints projected on the (m_χ, λ_L) and (m_χ, λ_A) planes respectively. In our analysis, we do not specify S or A must be a LOP before the scan. We tolerate either $\chi = S$ or $\chi = A$ can be the LOP, fixed only by each model point in the parameter space surviving the imposed constraints during the scan. By comparison of the upper left panel and the two lower panels of Fig. 5, one can identify the two regions of $|\lambda_{\chi\chi}| \leq 0.02$ with small $m_\chi \leq 110$ GeV and of $|\lambda_{\chi\chi}| \leq 1.2$ with large $m_\chi \geq 500$ GeV in which $\lambda_L > \lambda_{\chi\chi} = \lambda_A$ and hence $\chi = A$ being the LOP. Other regions in the upper left panel will have $\chi = S$ being the LOP. Similar behaviors for λ_A and m_χ can be found from the projected (m_χ, λ_A) plane in the upper right panel of Fig. 5, when comparing with the two lower panels. The small differences seen from the two plots in the upper panel of Fig. 5 near the Higgs resonance region can be traced back to the fact that we take λ_L as input parameter while λ_A as output parameter, given by a combination of λ_L , m_S and m_A via Eq. (11). From Eq. (11), we can see that when S is the LOP, λ_5 is negative so that λ_A is greater than λ_L . On the other hand, $\lambda_A < \lambda_L$ if A is the LOP. Therefore, λ_A will always have a wider range than λ_L . From the two plots in the upper panel of Fig. 5, one can see that for **RC** constraints the allowed parameter space of λ_L is also highly restricted compared to that of λ_A . The additional parameter space for λ_A at Higgs resonance appears only if A is the NLOP. Because of $m_A - m_S > 10$ GeV, the λ_A coupling being an output parameter according to Eq. (11) implies a very low abundance of A and therefore is not very sensitive to the relic density likelihood function.

Generally speaking, the allowed ranges of λ_L and λ_A for a given mass range of m_χ can be similar (but not identical) if one allows either S or A to be the LOP. We illustrate this further using the two plots in the lower panel of Fig. 5 where the profile likelihood on the $(m_\chi, \lambda_{\chi\chi})$ is shown, with left and right panels for $m_\chi \leq 100$ GeV and $m_\chi \geq 500$ GeV respectively. In these two plots, we can see that the 95% confidence level regions for the **RC** constraints applied in the $(m_\chi, \lambda_{\chi\chi})$ plane are mostly symmetric but with some small asymmetries, especially in the small mass region of $m_\chi \leq 100$ GeV. In the lower left plot of Fig. 5 where $65 < m_\chi < 100$ GeV, a negative $\lambda_{\chi\chi}$ is required to guarantee the cancellation between the contributions from different diagrams in the W^+W^- (or ZZ) channel such that a correct relic abundance can be achieved [25]. From these two profile likelihood plots on the $(m_\chi, \lambda_{\chi\chi})$ plane, three different limits on

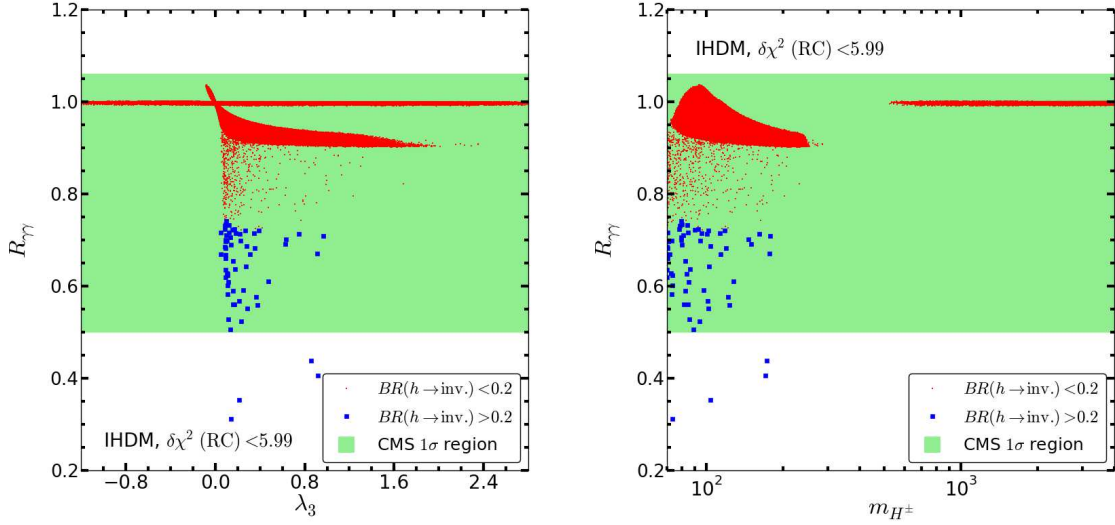


FIG. 6: The two dimension scatter plots on the $(\lambda_3, R_{\gamma\gamma})$ plane (*left*) and the $(m_{H^\pm}, R_{\gamma\gamma})$ plane (*right*). The blue squares and the red dots correspond to $BR(h \rightarrow \text{invisible}) > 0.2$ and < 0.2 respectively.

$\lambda_{\chi\chi}$ can be summarized as follows:

- $m_\chi \leq 63$ GeV: The upper limit of $\lambda_{\chi\chi}$ in this region is due to the invisible Higgs boson decay width being too large. This limit is roughly $|\lambda_{\chi\chi}| \leq 0.026$. The impact from the current monojet data is not strong. We have checked that it can constrain $|\lambda_{\chi\chi}|$ from $0.03 - 0.026$.
- $63 \leq m_\chi \leq 95$ GeV: Since the invisible Higgs boson decay is closed in this mass range, the $\lambda_{\chi\chi}$ can be in the range $-0.16 \leq \lambda_{\chi\chi} \leq 0.02$ ⁶.
- $m_\chi \geq 500$ GeV: As seen in Fig. 4, the relic density reduction at $m_\chi > 500$ GeV region is mainly resulting from the $S - A$, $S - H^\pm$ and $A - H^\pm$ coannihilation. In addition, the W^+W^- final state is being suppressed by increasing m_χ . Therefore, we can see $\lambda_{\chi\chi}$ is increasing with respect to m_χ in order to maintain correct relic density. The limit depends on m_χ and is in the range of $|\lambda_{\chi\chi}| \leq 1.1$. The upper limit increases for higher m_χ . One can work out these lower limits from the theoretical constraints, Eqs. (14) and (20).

⁶ It is worthy of mentioning that if we relax the relic density constraint to 3σ region, this strip will be extended to $m_\chi \sim 110$ GeV which is consistent with Ref. [24, 25].

C: Fig. 6

Third and last for this subsection of **RC**, we discuss the diphoton signal strength constraint from the LHC. As reported by many studies, most of the ATLAS and CMS data are consistent with SM predictions. However, there are some small discrepancies between ATLAS and CMS results as far as the diphoton channel is concerned. While the ATLAS result shows some small excesses with respect to SM value, the CMS result which is based on multivariate analysis is nevertheless consistent with SM. Here, we do not tempt to explain the ATLAS excess by the additional charged Higgs boson loops in IHDM but instead we would like to show the points that satisfy $\delta\chi^2 < 5.99$.

It is well known that in the SM, $h \rightarrow \gamma\gamma$ is dominated by W^\pm loops which interfere destructively with the subdominant top quark loop. In IHDM, the charged Higgs boson loops can be constructive or destructive with the W^\pm contributions depending on whether $\lambda_3 < 0$ or $\lambda_3 > 0$ respectively [27, 28]. As we showed before $R_{\gamma\gamma}$ in the present case can be reduced to the ratio of the IHDM and SM branching ratios (see Eq. (23)). Thus once the invisible decay $h \rightarrow \chi\chi$ is open, as long as the partial width of $h \rightarrow \gamma\gamma$ has a comparable size with the SM one, the ratio $R_{\gamma\gamma}$ will always be suppressed, *i.e.* $R_{\gamma\gamma} \approx \Gamma_{\text{SM}}(h)/(\Gamma_{\text{SM}}(h) + \Gamma(h \rightarrow \chi\chi)) < 1$.

In the left and right panels of Fig. 6 we present the signal strength $R_{\gamma\gamma}$ as a function of the coupling between the SM Higgs boson and a pair of charged Higgs bosons $g_{hH^\pm H^\mp} = -v\lambda_3$ and of the charged Higgs boson mass respectively. The green band indicates the CMS result with 1σ uncertainty. In both panels of Fig. 6, we have the blue and red dots for the branching ratio of the invisible Higgs boson decay being larger and smaller than 20% respectively. On the other hand, if the invisible decay is close, one can see some small enhancements of $R_{\gamma\gamma} > 1$ for negative λ_3 (left panel). Taking the relic density within 2σ range from Eq. (24) as well as the invisible decay branching ratio to be less than 65% (with 11.18% uncertainty obtained by adding in quadrature the experimental and theoretical errors given in Table I), we find that $R_{\gamma\gamma}$ falls in the range 0.3 to 1.04. This upper limit of 1.04 for $R_{\gamma\gamma}$ from the relic density constraint was already reported in [27, 28]. Most of the points are within CMS 1σ band except for a few points with branching ratio of the Higgs invisible decay larger than 20% which are already excluded. Overall, our results agree with Ref. [24].

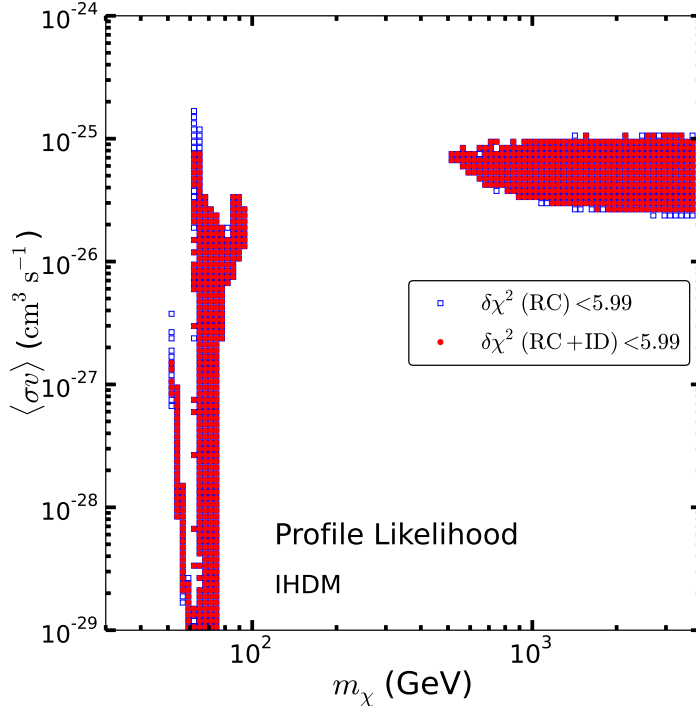


FIG. 7: The two dimension profile likelihood on the $(m_\chi, \langle\sigma v\rangle)$ plane. The blue squares are 2σ allowed region by **RC** constraints and the red dots are 2σ allowed region by **RC+ID** constraints.

2. **RC+ID**

We now move on to study the impact of DM indirect detection on the parameters m_χ and velocity averaged annihilation cross section $\langle\sigma v\rangle$, where v is the relative velocity of the annihilating DM. Nowadays, the DM relative velocity is non-relativistic, one can simply use the approximation $\langle\sigma v\rangle = \sigma v|_{v \rightarrow 0}$. In Fig. 7, we show the two dimensional profile likelihood on the $(m_\chi, \langle\sigma v\rangle)$ plane. The blue squares are 2σ allowed region by **RC** constraints and the red dots are 2σ allowed region by **RC+ID** constraints.

First, we can see three main branches, two vertical branches at $2m_\chi \sim m_h$ region and one horizontal at $m_\chi \gtrsim 500$ GeV region. They are corresponding to two different mechanisms to produce the correct relic density as discussed before. Comparing with Fig. 4, the first vertical branch at $m_\chi < 60$ GeV is $S - A$ coannihilation but the second vertical branch at $60 \text{ GeV} < m_\chi < 100$ GeV is Higgs resonance region plus the openings of the W^+W^- and ZZ channels. The horizontal branch is again the coannihilation region. The thermal averaged $\langle\sigma v\rangle_T$ of the vertical branches are more p -wave (velocity dependent) so that most of the

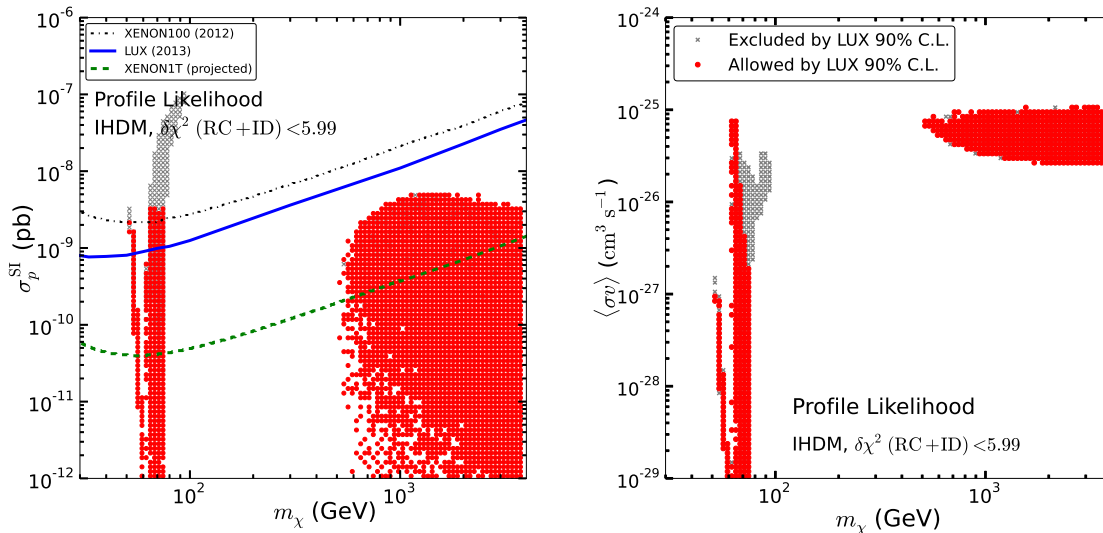


FIG. 8: The two dimension profile likelihood on the $(m_\chi, \sigma_p^{\text{SI}})$ plane (*left*) and the $(m_\chi, \langle\sigma v\rangle)$ plane (*right*). All points (both red and gray colors) satisfy **RC+ID** constraints in 2σ . The regions of gray crosses in both panels are excluded in 2σ level by LUX where the uncertainty on the hadronic matrix elements is taken into account, while the regions of red dots are allowed. The theoretical uncertainty on LUX can weaken the experimental limit so that the red dotted region in the left panel can overshoot the LUX (or even XENON100) limit in the Higgs resonance region.

points can have wider spread values of $\langle\sigma v\rangle$. On the other hand, the horizontal branch is more s -wave (velocity independent) so that $\langle\sigma v\rangle \sim \text{a few} \times 10^{-26} \text{ cm}^3 \cdot \text{s}^{-1}$.

Clearly, we can see that at the low m_χ region (the two vertical branches) where the IHDM DM has larger $\langle\sigma v\rangle$ the constraints from **ID** can further reduce the parameter space from the **RC** block only. In the first branch, **ID** constraints can even make $\langle\sigma v\rangle$ having a value as low as $10^{-27} \text{ cm}^3 \cdot \text{s}^{-1}$.

3. **RC+DD+ID**

On top of the **RC+ID** constraints, we can further include the **DD** constraint from LUX. In the left panel of Fig. 8, the 2σ allowed region on the $(m_\chi, \sigma_p^{\text{SI}})$ plane by **RC+DD+ID** constraints is shown in red circles. The region of gray crosses was excluded by the LUX result with the hadronic uncertainties included. In IHDM, only t -channel with the h exchange can contribute to DM-quark elastic scattering. Therefore, one can expect the gray crosses region

is due to the coupling $\lambda_{L,A}$ being too large. Interestingly, in the right panel where we map to the $(m_\chi, \langle\sigma v\rangle)$ plane, we can see that the LUX limit can only remove some regions (gray crosses) with low m_χ which have large σ_p^{SI} (left panel) but the region (red dots) with $\langle\sigma v\rangle$ as high as $8 \times 10^{-26} \text{ cm}^3 \cdot \text{s}^{-1}$ is still allowed! In addition, in the left pane we also plot the projected sensitivity of XENON1T which has the potential to probe the higher mass coannihilation region. We will discuss this impact further in section VII.

In Fig. 9, we show the 1D relative likelihood distributions for m_S (upper left), m_χ (upper right), m_{H^\pm} (lower left) and $\lambda_{\chi\chi}$ (lower right) in the three blocks of **RC**, **RC+ID**, and **RC+ID+DD**, marked by black dash-dot, blue dash, and red solid lines, respectively. The relative likelihood in each case is defined as $\mathcal{L}/\mathcal{L}_{\text{max}}$ where \mathcal{L}_{max} is the likelihood at the best-fits. We do not show the distribution of m_A since it is almost identical to m_S . As aforementioned that m_χ can be either m_S or m_A , the peaks at $m_\chi < 100 \text{ GeV}$ in the upper right panel correspond actually to two separated peaks with almost the same height at $m_S < 300 \text{ GeV}$ in the upper left panel. The first peak owes to $m_\chi = m_S$ and the second $m_\chi = m_A$. We can see clearly that there is no preference of $m_\chi = m_A$ or $m_\chi = m_S$.

Since the $\gamma/e^+/\bar{p}$ fluxes are inversely proportional to m_χ^2 , the impact of **ID** constraint is mainly on the lower m_χ region. On the other hand, if m_χ turns out to be too large suppressing the DM signal, the total **ID** χ^2 will be the same as consideration of background only. From Fig. 9, we found that with the additional DM signal, the χ^2 can be improved to at most 1σ significance. For example, in the upper right plot, we can see that at the $m_\chi > 500 \text{ GeV}$ region there is a flat **RC** likelihood distribution while the **RC+ID** one is decreasing. Because of $\chi - H^\pm$ coannihilation, we can see similar decrease of the **RC+ID** likelihood distribution for the $m_{H^\pm} > 500 \text{ GeV}$ region in the lower left plot. Note that this large m_χ region can not be constrained by the current LUX data. There is a third peak at $m_\chi \sim 500 \text{ GeV}$ because the $m_\chi < 100 \text{ GeV}$ region is less favored by LUX. Even though the best-fit point still locates at this lower mass region, the minimum χ^2 is roughly increased by one unit. As a result of increasing the minimum χ^2 , the relative likelihood of the $m_\chi > 500 \text{ GeV}$ region becomes statistically more significant.

In Table II, we show the results of some of the basic parameters and observables in the **RC+ID+DD** block at a few benchmark points. These benchmark points correspond to the main mechanisms that reduce the relic density, namely the $S - A$ coannihilation, Higgs resonance, $S - A - H^\pm$ ($S - A$ and $\chi - H^\pm$) coannihilation, and $S - H^\pm$ coannihilation.

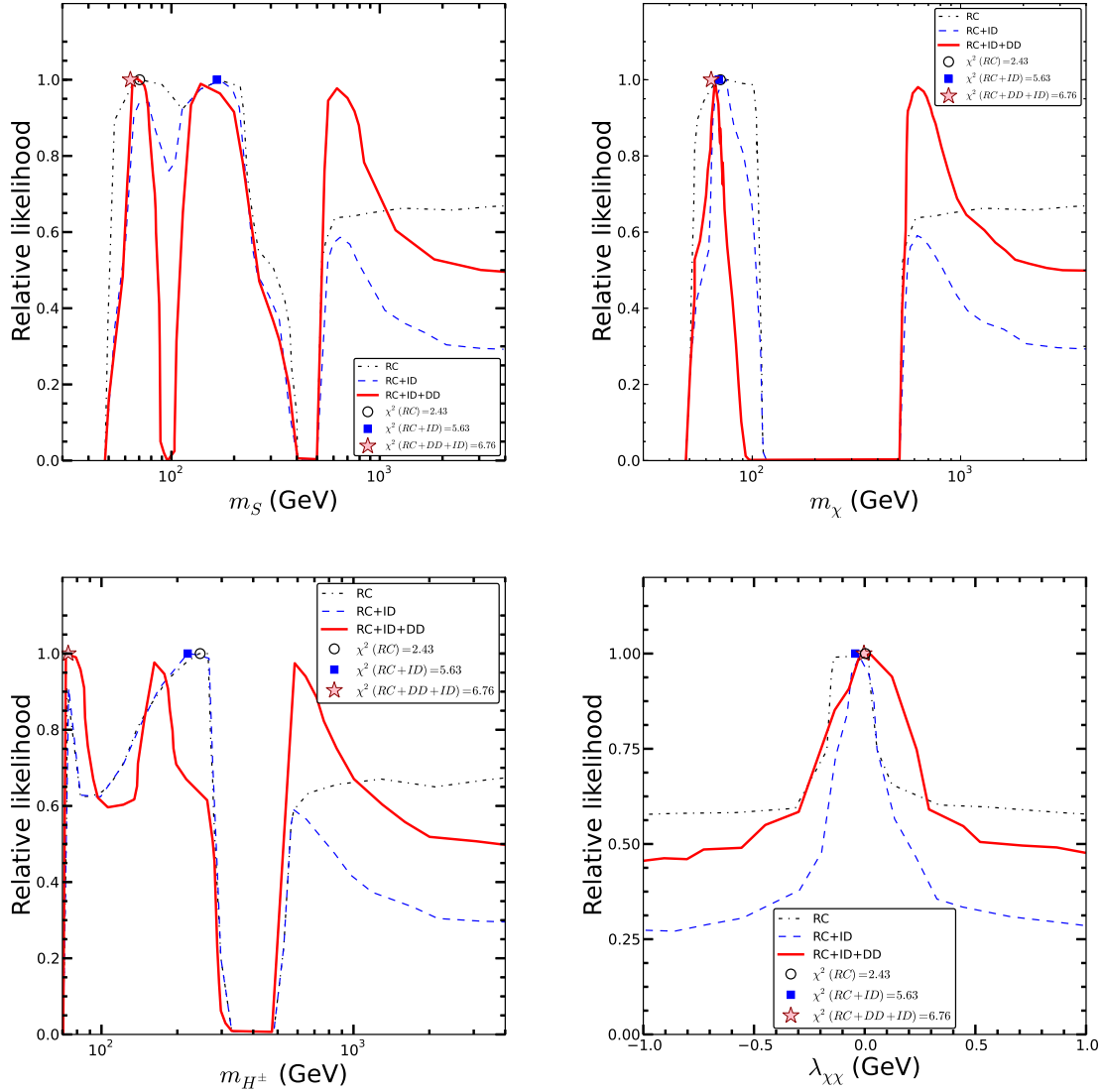


FIG. 9: One-dimensional profile likelihood distribution for m_S , m_χ , m_{H^\pm} , and DM effective coupling $\lambda_{\chi\chi}$. The distribution of m_A is almost identical to m_S . The best-fits are presented by black circles, blue squares, and red stars for the three likelihood combination blocks, **RC**, **RC+ID**, and **RC+DD+ID**, respectively.

Moreover, these four mechanisms can also represent four different relevant m_χ regions. For the two columns of the $S - A$ coannihilation and Higgs resonance in Table II, the $b\bar{b}$ final state plays an important role in the annihilation channels. However, as long as the W^+W^- and ZZ channels are open, they will contribute significantly to the annihilation cross section, as clearly seen in the last two columns of this table. One may notice that in the last column

	$S - A$ Co-ann.	Higgs Resonance	$S - A - H^\pm$ Co-ann.	$S - H^\pm$ Co-ann.
Basic Parameters				
m_h (GeV)	125.6	125.92	126.51	125.44
m_S (GeV)	70.17	64.46	522.13	971.88
m_A (GeV)	78.55	130.83	521.98	985.56
m_{H^\pm} (GeV)	97.47	76.11	523.27	979.49
λ_L	-0.032	-0.009	-0.052	-0.248
λ_2	0.60	9.3×10^{-4}	1.61	2.81
DM Observables				
$\Omega_\chi h^2$	0.107	0.123	0.105	0.097
$\langle \sigma v \rangle$ ($\text{cm}^3 \cdot \text{s}^{-1}$)	9.81×10^{-27}	2.14×10^{-26}	7.51×10^{-26}	4.58×10^{-26}
σ_p^{SI} (pb)	7.11×10^{-9}	6.96×10^{-10}	3.59×10^{-10}	2.62×10^{-9}
Channels Contributed to $1/\Omega h^2$				
Dominant	$SA \rightarrow q\bar{q}$ (41%)	$SS \rightarrow b\bar{b}$ (49%)	$SS/AA/H^+H^- \rightarrow W^+W^-$ (39%)	$H^\pm H^\pm \rightarrow W^\pm W^\pm$ (16%)
Subdominant	$SS \rightarrow b\bar{b}$ (31%)	$SH^\pm \rightarrow \gamma W^\pm$ (17%)	$SS/AA/H^+H^- \rightarrow ZZ$ (21%)	$SS \rightarrow W^+W^-, ZZ, hh$ (9%,15%,14%)
			$SH^\pm/AH^\pm \rightarrow W^\pm \gamma/W^\pm Z$ (21%)	$SH^\pm \rightarrow W^\pm Z, W^\pm h$ (6%,9%)
ID Annihilation Cross Section $\langle \sigma v \rangle$				
Dominant	$SS \rightarrow b\bar{b}$ (75%)	$SS \rightarrow b\bar{b}$ (77%)	$AA \rightarrow W^+W^-$ (51%)	$SS \rightarrow ZZ$ (39%)
Subdominant	$SS \rightarrow gg$ (12%)	$SS \rightarrow gg$ (10%)	$AA \rightarrow ZZ$ (44%)	$SS \rightarrow hh$ (36%)
Pulls for ID Observables				
$\delta\chi_{\gamma, \text{dSphs}}^2$	0.83	0.22	1.05	1.99
$\delta\chi_{\gamma, \text{GC}}^2$	0.87	0.61	0.88	0.93
$\delta\chi_{e^+}^2$	0.38	0.25	0.19	0.49
$\delta\chi_p^2$	0.62	1.17	0.04	0.15

TABLE II: Values of some **RC+ID+DD** parameters and observables as well as the $\delta\chi^2$ for the **ID** observables at several benchmark points.

of $S - H^\pm$ coannihilation case, the distribution of different channels contributed to the relic density is quite spread out in this case. Thus, beside the Higgs resonance point, the other coannihilation channels can lead to effective relic density reduction as well. Finally, we also show in Table II the **ID** $\delta\chi^2$ for these four benchmark points. We note that poorer values of $\delta\chi_p^2$ are obtained at the first two benchmark points ($S - A$ coannihilation and Higgs resonance) where the $b\bar{b}$ final state dominates in the antiproton flux. While the $b\bar{b}$ mode can be significant for the antiproton flux from the fragmentation of b and \bar{b} into antiproton, the smallness of the b -quark parton distribution inside the nucleon makes the b -quark has very small impact on the σ_p^{SI} . On the other hand, values of σ_p^{SI} at these two benchmark points are quite acceptable.

In Table III, we summarize the best-fit points for the three different blocks from our scan. The second column is only with **RC** constraints in the likelihood while the third and fourth

Parameter	$\mathcal{L}(\mathbf{RC})$	$\mathcal{L}(\mathbf{RC+ID})$	$\mathcal{L}(\mathbf{RC+DD+ID})$
m_h (GeV)	125.76	125.91	126.016
m_S (GeV)	70.37	165.12	63.54
m_A (GeV)	196.58	69.04	166.16
m_{H^\pm} (GeV)	246.28	219.85	73.78
λ_L	2.96×10^{-3}	0.33	-3.29×10^{-3}
λ_2	3.50	3.58	5.67×10^{-4}
$\langle\sigma v\rangle$ ($\text{cm}^3 \cdot \text{s}^{-1}$)	7.97×10^{-28}	2.44×10^{-26}	2.18×10^{-26}
σ_p^{SI} (pb)	5.92×10^{-11}	1.22×10^{-8}	8.89×10^{-11}
χ^2	2.43	5.63	6.76

TABLE III: Table displaying the properties of our best-fit points for the three different blocks. Note that the invisible Higgs decay is closed at these three best-fit points.

columns are with **RC+ID** and **RC+DD+ID** in the likelihood, respectively. We would like to stress that there is no preference of $\chi = S$ or $\chi = A$ due to the symmetry between S and A in the model. We find that the maximum likelihood of $\mathcal{L}(\chi = S)$ and $\mathcal{L}(\chi = A)$ are roughly the same. Therefore, the fact that the best-fit points are located at $\chi = S$ or $\chi = A$ region is just due to the fact that we collected the maximum likelihood before hitting the sampling stop criteria. In other words, we cannot tell the dark matter in IHDM must be a scalar or pseudoscalar from this analysis. However, we can see that the best-fit points of three sets of constraint are all located at the lower m_χ region. The reasons for this are mainly due to the EWPT and indirect detection constraints. First, the nearly degeneracy between m_{H^\pm} and m_χ required by relic density constraints at the $m_\chi > 500$ GeV region implies S and T are always negligible. On the other hand, S and T can be enhanced in the $m_\chi \lesssim 100$ GeV region due to larger mass splitting between H^\pm and χ . Hence, we can obtain the better likelihood in small m_χ region. Second, the lower m_χ region may amplify the indirect detection signal too, because the signal fluxes of indirect detection experiments are inversely proportional to m_χ^2 . Hence, lower m_χ region can have stronger signals to fit current **ID** constraints than astrophysical background only. On the other hand, the fluxes from DM annihilation in the $m_\chi > 500$ GeV region can be suppressed and may be lower

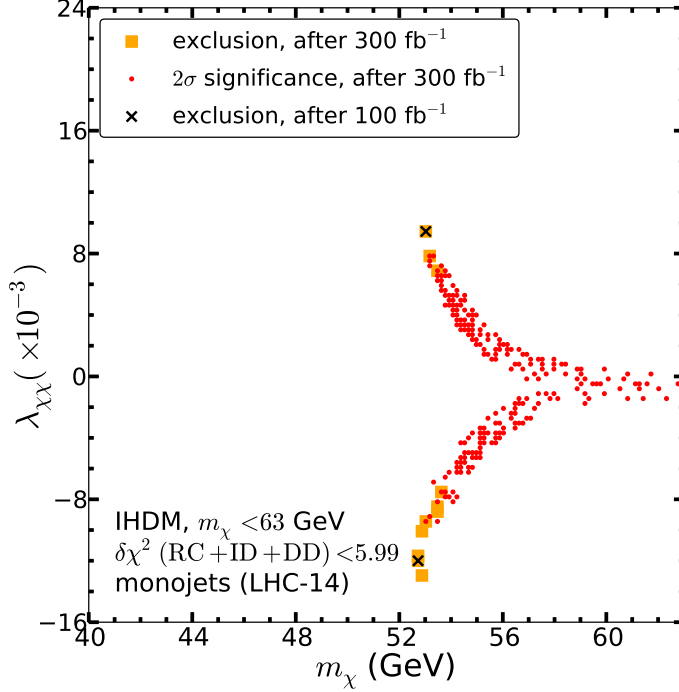


FIG. 10: The 2σ profile likelihood of the **RC+ID+DD** constraints projected on the $(m_\chi, \lambda_{\chi\chi})$ plane for the monojet result at LHC-14. The black crosses will be excluded by the future 100 fb^{-1} data. The orange square will still be allowed by 100 fb^{-1} data but disfavoured by 300 fb^{-1} data. The red dots will be allowed by 300 fb^{-1} data. They are all in 2σ significance.

than the astrophysical background. As seen from Figs. 1 and 2, there are still some rooms for DM in indirect detection experiments. Perhaps not a discovery with large statistical significance, but a weak signal usually fits the likelihood better than using the background only hypothesis. Certainly, our understandings of the astrophysical backgrounds could be too naive.

VII. FUTURE EXPERIMENTAL CONSTRAINTS FROM LHC-14, XENON1T AND AMS-02

In this section, we will consider the sensitivities of three future experiments: (1) LHC-14 monojet with luminosities 100 fb^{-1} and 300 fb^{-1} , (2) XENON1T, and (3) AMS-02 one year antiproton data, given the parameter space obtained in previous section that satisfies the

RC+DD+ID constraints.

A. LHC-14 monojet

At the 14 TeV run of LHC (LHC-14), we will discuss the impact of the monojet search with luminosities of 100 fb^{-1} and 300 fb^{-1} . We assume a null measurement of DM with background events same as observed, *i.e.* $b = o$ where b and o are the background and observed events at 100 fb^{-1} or 300 fb^{-1} obtained by scaling the current CMS data at luminosity of 19.5 fb^{-1} . Using the standard sensitivity formula, s/\sqrt{b} , we compute the significance of monojet for LHC-14.

In Fig. 10, we present the potential power of LHC monojet search with 100 fb^{-1} and 300 fb^{-1} on the $(m_\chi, \lambda_{\chi\chi})$ plane. In linear scale, we zoom into the region $m_\chi < 63 \text{ GeV}$ where the invisible Higgs decay is open. All the points shown satisfy the **RC+DD+ID** constraints in 2σ . With 100 fb^{-1} of data, only the orange boxes will be allowed while the few black crosses located near the boundary where $|\lambda_{\chi\chi}| \sim 10^{-2}$ will be disfavoured in the 2σ subset. However, with 300 fb^{-1} of data, the range of $\lambda_{\chi\chi}$ will be extended to the region of red dots in Fig. 10 where $|\lambda_{\chi\chi}| \lesssim 6 \times 10^{-3}$.

B. XENON1T

In Fig. 11, we show the disfavoured region by future XENON1T sensitivities subjected to the **RC+ID+DD** constraints in 2σ significance. The left panel is for $(m_\chi, \lambda_{\chi\chi})$ and the right panel is for $(m_\chi, \langle\sigma v\rangle)$. The red dots are favoured but gray dots/crosses are disfavoured by XENON1T limit. Although the region of $m_\chi > 500 \text{ GeV}$ can not be entirely ruled out by XENON1T from our global analysis based on tree level calculation, a recent paper [89] pointed out that electroweak corrections can significantly alter the theoretical prediction of σ_p^{SI} , especially for large m_χ region. As shown in their computation, σ_p^{SI} is not expected to be lower than 10^{-11} pb even when one loop corrections are included [89]. We thus expect next generation of ton-sized detectors for DM direct detection can probe most of the parameter space of IHDM.

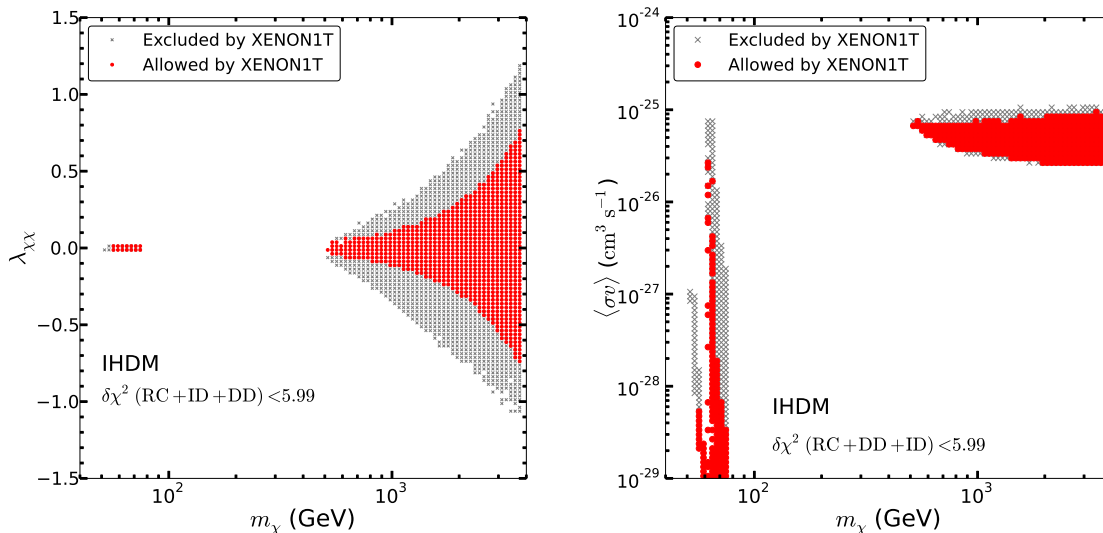


FIG. 11: The left and right panels show the sensitivity of XENON1T on the $(m_\chi, \lambda_{\chi\chi})$ and $(m_\chi, \langle\sigma v\rangle)$ planes respectively subjected to the **RC+ID+DD** constraints in 2σ significance. The red (gray) area will be allowed (excluded) by XENON1T sensitivity.

C. AMS-02 antiproton

We generate the simulated one year AMS-02 data of the antiprotons following Ref. [90]. The expected antiproton flux ϕ is adopted to be the one described in section II (see Fig. 2). The number of antiproton events in a given energy bin is approximately

$$N_{\bar{p}}(E_k) = \Delta t \int_{\Delta E} dE_k \phi(E_k) \times A(E_k), \quad (34)$$

where $A(E_k)$ is the simulated geometry factor given in [91], ΔE is the width of the energy bin and Δt is the exposure time. We generate the data from 1 to 300 GeV, with 50 bins logarithmically evenly distributed according to the binning of the positron fraction measurement by AMS-02 [37]. For the “observed” number of events we apply a Poisson fluctuation on $N_{\bar{p}}$, with statistical error $\approx 1/\sqrt{N_{\bar{p}}}$. The systematic error is simply adopted to be $\sim 5\%$ [90], which is added quadratically to the statistical error. The simulated antiproton flux for one year observation of AMS-02 is shown in the left panel of Fig. 12. Using the simulated antiproton data, we calculate the χ^2 of each DM model point with the same method described in sections IV and V. In the right panel of Fig. 12, the exclusion power of the AMS-02 one year antiproton data is shown. The red dots are allowed but gray crosses are disfavoured

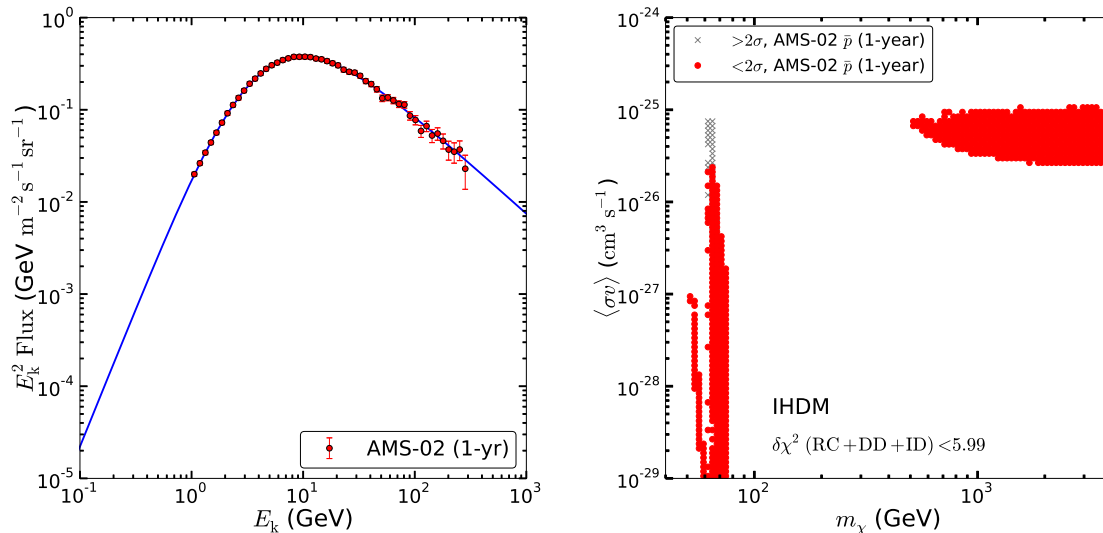


FIG. 12: Simulated antiproton flux for one year observation of AMS-02 (*left*). The AMS-02 antiproton one year sensitivity on the $(\langle\sigma v\rangle, m_\chi)$ plane (*right*). The red dots (gray crosses) will be allowed (excluded) by AMS-02 anti-proton one year sensitivity.

by future sensitivity. Comparing with the exclusion power of XENON1T sensitivity (right panel of Fig. 11), we can see most of parameter space excluded by AMS-02 antiproton data are also excluded by XENON1T. However, for the $\langle\sigma v\rangle \sim 2 \times 10^{-26} \text{cm}^3 \cdot \text{s}^{-1}$ at the Higgs resonance region (near the top of the second vertical branch from the left), one can find some small fractions of red dots that can be excluded by AMS-02 antiproton data but not yet ruled out by XENON1T. This is because the DM annihilation channels are dominant by $\tau^+\tau^-$ or $b\bar{b}$ final state at these points. However the $h\tau^+\tau^-$ coupling is irrelevant to direct detection and the $hb\bar{b}$ coupling can contribute to direct detection only by integrating this heavy b quark to obtain the hgg coupling. Hence its contributions to σ_p^{SI} is also small as compared with light quarks.

D. LHC-14 Monojet + XENON1T + AMS-02 antiproton flux

We finally show in Fig. 13 the total impact from the combined sensitivities from the above three future experiments on the $(m_\chi, \lambda_{\chi\chi})$ plane. For the LHC-14 monojet, we will assume 300 fb^{-1} of data in making these two plots. Left and right panels correspond to m_χ less than 100 GeV and greater than 500 GeV respectively. With all three future experiments

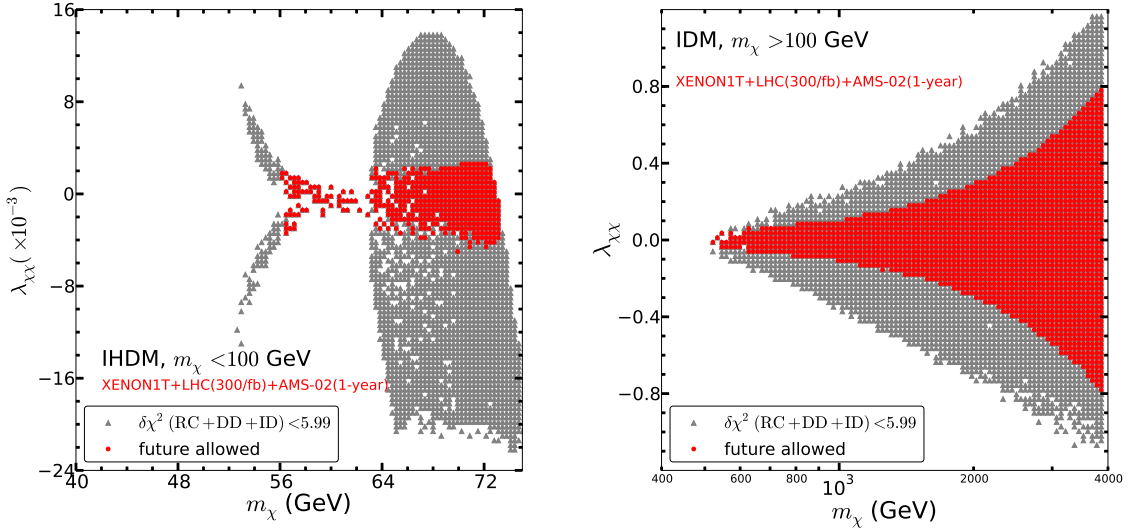


FIG. 13: The scatter plots to present the future combined sensitivity from XENON1T, LHC-14 monojet (300 fb^{-1}), and AMS-02 antiproton flux measurements on (m_χ, λ_L) plane subjected to the **RC+ID+DD** constraints in 2σ significance. The left and right panels are for $m_\chi < 100 \text{ GeV}$ and $m_\chi > 500 \text{ GeV}$ respectively.

sensitivities, from the left panel of a zoomed-in view of low m_χ region, we see that the lower limit of m_χ is lifted slightly from 52 GeV to 55 GeV . In this low mass region where the invisible decay $h \rightarrow \chi\chi$ is open, while we do not found any upper limit on m_χ , $\lambda_{\chi\chi}$ is found to lie between -5×10^{-3} and 3×10^{-3} . On the other hand, if the invisible mode is closed, the upper and lower limit of $\lambda_{\chi\chi}$ is varied with respect to m_χ (right panel). Comparing with current experimental data, these three future experiments sensitivities are robust but neither the lower m_χ region nor the larger m_χ region can be entirely ruled out.

VIII. CONCLUSIONS

Despite IHDM was proposed more than three decades ago, it is still one of the most simplest models and yet viable for scalar dark matter. We have performed a global fit analysis on this model. This analysis has been performed in light of the recent ATLAS and CMS discovery of a $125\text{-}126 \text{ GeV}$ Higgs-like particle, taking into account the recent relic density measurement by PLANCK, DM direct detection from LUX and indirect detection from PAMELA, Fermi-LAT and AMS-02.

We have shown that the constraint from DM direct detection search, such as the latest LUX upper limit of year 2013, provides a robust constraint on the parameter space. In particular, if the invisible decay of the SM Higgs boson is open, the upper limit of the Higgs invisible width from LHC together with the LUX constraint could put some interesting limits on the SM Higgs boson couplings to the DM in IHDM. Indeed, an invisible decay of the SM Higgs boson with a branching ratio larger than 30% and a scalar dark matter mass within the range of 20-60 GeV are excluded by current data.

We emphasize that there is no preference of $\chi = S$ or A in our study. However, we found that $m_\chi \lesssim 100$ GeV region is slightly favoured by EWPT and **ID** constraints than $m_\chi \gtrsim 500$ GeV region. In addition, in the 95% C.L. of **RC+DD+ID** constraints, m_χ has the lower limit around 52 GeV.

The exclusion power of the AMS-02 one year antiproton data on the model parameters can be inferred from Figs. 12 and 13. The results show that AMS-02 does have the potential to constrain certain parameter space of IHDM, especially in the low mass region. However, compared with the direct detection limit expected from XENON1T, the constraint from AMS-02 antiproton data is weaker as comparing the two Figs. 11 and 12.

Nevertheless, future data from LHC-14 monojet, XENON1T direct detection and AMS-02 antiproton flux can further reduce the IHDM parameter space constrained by the existing **RC+DD+ID** data, as is shown inevitably in the red regions as compared with the gray regions in the two plots at the left and right panels of Fig. 13 for the low and high DM mass regions respectively.

We also note that the likelihoods obtained in this work were obtained using the tree level relation for λ_L and λ_A (Eq. (11)) and the tree level formula for the coupling $g_{h\chi\chi}$ (Eq. (13)). Higher order corrections will necessarily modify these relations and hence the relic density prediction will be affected. The profile likelihoods for the IHDM will be modified as well. Although loop corrections have been shown to affect significantly the DM scattering cross-section on nucleons in the IHDM [89] and thus modify the impact of direct detection searches on the viable parameter space of the model, it is beyond the scope of the present analysis to take them into account. One should bear in mind that such corrections will also probably affect the positions of the best-fit points.

In summary, we note that the overall shapes of the 95% C.L. contours presented in this work are mainly determined by the PLANCK relic density measurement. LHC monojet is

only relevant when the invisible decay of the Higgs is open, in which case we obtain the limit for the coupling $\lambda_{L,A} \approx 10^{-1}$ which is not very stringent. On the other hand, our best-fit points are located at $m_\chi \approx 70$ GeV and so do not allow the opening for invisible decay of the SM Higgs into DM. The current **ID** and **DD** data are only sensitive to Higgs resonance region. Except for relic density constraint, currently no other experimental data sets are sensitive to the IHDM parameter space at $m_\chi \gtrsim 500$ GeV. However, one expects future XENON1T can probe this region. Moreover, future instruments such as DAMPE, GAMMA-400 and CTA will test this higher m_χ region as well [92].

As mentioned previously, experimental search for the inert Higgs (neutral and charged) behaves like SUSY search for charginos and neutralinos. Therefore, one of the most popular signatures for inert Higgs searches would be also trilepton and/or dilepton plus missing E_T [30, 93]. A dedicated analysis for the IHDM has been performed in [30] where it has been demonstrated that the experimental reach for the inert Higgses is only about 300 GeV which is somewhat smaller than the LHC reach for the charginos and neutralinos. The main reason is that the cross section for the scalar pair production $pp \rightarrow H^\pm A^0$ is smaller than the gaugino pair production $pp \rightarrow \chi_1^\pm \chi_2^0$. As we have seen in our analysis, inert Higgses with masses $\geq 0.5 - 4$ TeV are consistent with all experimental and theoretical constraints. One concludes that the IHDM is here to stay for another decade.

The IHDM can be further extended by including inert right-handed neutrinos with Majorana masses [16]. Masses for the SM light neutrinos can be generated through radiative processes with only inert particles running inside the loop. This extension of IHDM would exhibit intricate interplay between dark matter and neutrino physics. Detailed global analysis of this extended model is also quite interesting and will be presented in a future publication.

Acknowledgments

AA would like to thank the National Science Council (NSC) of Taiwan for financial support during his stay at the Institute of Physics (IOP), Academia Sinica (AS). ST would like to thank the hospitality and support from the High Energy Theory Group at the IOP, AS. This work is supported by National Natural Science Foundation of China under grant number 11105155 (QY) and by the NSC of Taiwan under project number 102-2811-M-001-032 (AA) and grant number 101-2112-M-001-005-MY3 (TCY).

-
- [1] G. Aad *et al.* [ATLAS Collaboration], Phys. Lett. B **716**, 1 (2012) [arXiv:1207.7214 [hep-ex]].
 - [2] S. Chatrchyan *et al.* [CMS Collaboration], Phys. Lett. B **716**, 30 (2012) [arXiv:1207.7235 [hep-ex]].
 - [3] T. Aaltonen *et al.* [CDF and D0 Collaborations], Phys. Rev. Lett. **109**, 071804 (2012) [arXiv:1207.6436 [hep-ex]]; Phys. Rev. D **88**, 052014 (2013) [arXiv:1303.6346 [hep-ex]].
 - [4] G. Aad *et al.* [ATLAS Collaboration], Phys. Lett. B **726**, 88 (2013) [arXiv:1307.1427 [hep-ex]]; ATLAS-CONF-2013-079, 19-July-2013.
 - [5] S. Chatrchyan *et al.* [CMS Collaboration], JHEP **06**, 081 (2013) [arXiv:1303.4571 [hep-ex]]; CMS-PAS-HIG-13-005, 17-April-2013.
 - [6] [CMS Collaboration], CMS-PAS-HIG-12-045; [The ATLAS & CMS Collaborations], ATLAS-CONF-2011-157/CMS-PAS-HIG-11-023.
 - [7] D. Carmi, A. Falkowski, E. Kuflik and T. Volansky, JHEP **1207**, 136 (2012) [arXiv:1202.3144 [hep-ph]]; A. Azatov, R. Contino and J. Galloway, JHEP **1204**, 127 (2012) [Erratum-ibid. **1304**, 140 (2013)] [arXiv:1202.3415 [hep-ph]]; M. Klute, R. Lafaye, T. Plehn, M. Rauch and D. Zerwas, Phys. Rev. Lett. **109**, 101801 (2012) [arXiv:1205.2699 [hep-ph]]; I. Low, J. Lykken and G. Shaughnessy, Phys. Rev. D **86**, 093012 (2012) [arXiv:1207.1093 [hep-ph]]; A. Azatov, S. Chang, N. Craig and J. Galloway, Phys. Rev. D **86**, 075033 (2012) [arXiv:1206.1058 [hep-ph]]; J. R. Espinosa, C. Grojean, M. Muhlleitner and M. Trott, JHEP **1205**, 097 (2012) [arXiv:1202.3697 [hep-ph]]; J. Ellis and T. You, JHEP **1209**, 123 (2012) [arXiv:1207.1693 [hep-ph]]; P. P. Giardino, K. Kannike, M. Raidal and A. Strumia, Phys. Lett. B **718**, 469 (2012) [arXiv:1207.1347 [hep-ph]].

- [8] G. Aad *et al.* [ATLAS Collaboration], arXiv:1307.1432 [hep-ex]; G. Aad *et al.* [ATLAS Collaboration]: ATLAS-CONF-2013-040.
- [9] S. Chatrchyan *et al.* [CMS Collaboration], Phys. Rev. Lett. **110**, 081803 (2013) [arXiv:1212.6639 [hep-ex]]; CMS-PAS-HIG-13-002.
- [10] N. G. Deshpande and E. Ma, Phys. Rev. D **18**, 2574 (1978).
- [11] For a review of the general two Higgs doublet models, see G. C. Branco, P. M. Ferreira, L. Lavoura, M. N. Rebelo, M. Sher and J. P. Silva, Phys. Rept. **516**, 1 (2012) [arXiv:1106.0034 [hep-ph]].
- [12] K. Cheung, J. S. Lee and P. -Y. Tseng, JHEP **1305**, 134 (2013) [arXiv:1302.3794 [hep-ph]].
- [13] G. Belanger, B. Dumont, U. Ellwanger, J. F. Gunion and S. Kraml, Phys. Lett. B **723**, 340 (2013) [arXiv:1302.5694 [hep-ph]].
- [14] G. Belanger, B. Dumont, U. Ellwanger, J. F. Gunion and S. Kraml, Phys. Rev. D **88**, 075008 (2013) [arXiv:1306.2941 [hep-ph]].
- [15] J. R. Espinosa, M. Muhlleitner, C. Grojean and M. Trott, JHEP **1209**, 126 (2012) [arXiv:1205.6790 [hep-ph]]; O. Lebedev, H. M. Lee and Y. Mambrini, Phys. Lett. B **707**, 570 (2012) [arXiv:1111.4482 [hep-ph]]; C. Englert, M. Spannowsky and C. Wymant, Phys. Lett. B **718**, 538 (2012) [arXiv:1209.0494 [hep-ph]].
- [16] E. Ma, Phys. Rev. D **73**, 077301 (2006) [hep-ph/0601225].
- [17] A. Arhrib, Y.-L. Sming Tsai, Q. Yuan and T. C. Yuan, work in progress.
- [18] V. Silveira and A. Zee, Phys. Lett. B **161**, 136 (1985).
- [19] K. Cheung, Y. -L. S. Tsai, P. -Y. Tseng, T. -C. Yuan and A. Zee, JCAP **1210**, 042 (2012) [arXiv:1207.4930 [hep-ph]].
- [20] J. McDonald, Phys. Rev. D **50**, 3637 (1994); C. P. Burgess, M. Pospelov and T. ter Veldhuis, Nucl. Phys. B **619**, 709 (2001); M. Cirelli, N. Fornengo and A. Strumia, Nucl. Phys. B **753**, 178 (2006).
- [21] M. C. Bento, O. Bertolami, R. Rosenfeld and L. Teodoro, Phys. Rev. D **62**, 041302 (2000); V. Barger, P. Langacker, M. McCaskey, M. J. Ramsey-Musolf and G. Shaughnessy, Phys. Rev. D **77**, 035005 (2008); M. Aoki, S. Kanemura and O. Seto, Phys. Rev. Lett. **102**, 051805 (2009) [arXiv:0807.0361 [hep-ph]]; Phys. Rev. D **80**, 033007 (2009) [arXiv:0904.3829 [hep-ph]].
- [22] K. Cheung and T. C. Yuan, Phys. Lett. B **685**, 182 (2010); X. G. He, T. Li, X. Q. Li, J. Tandean and H. C. Tsai, Phys. Lett. B **688**, 332 (2010); M. Farina, D. Pappadopulo

- and A. Strumia, Phys. Lett. B **688**, 329 (2010); M. Kadastik, K. Kannike, A. Racioppi and M. Raidal, Phys. Lett. B **685**, 182 (2010) [arXiv:0912.3797 [hep-ph]]; M. Aoki, S. Kanemura and O. Seto, Phys. Lett. B **685**, 313 (2010); M. Asano and R. Kitano, Phys. Rev. D **81**, 054506 (2010) [arXiv:1001.0486 [hep-ph]]; A. Bandyopadhyay, S. Chakraborty, A. Ghosal and D. Majumdar, JHEP **1011**, 065 (2010) [arXiv:1003.0809 [hep-ph]]; S. Andreas, C. Arina, T. Hambye, F. -S. Ling and M. H. G. Tytgat, Phys. Rev. D **82**, 043522 (2010) [arXiv:1003.2595 [hep-ph]].
- [23] M. Gustafsson, S. Rydbeck, L. Lopez-Honorez and E. Lundstrom, Phys. Rev. D **86**, 075019 (2012) [arXiv:1206.6316 [hep-ph]].
- [24] A. Goudelis, B. Herrmann and O. Stål, JHEP **1309**, 106 (2013) [arXiv:1303.3010 [hep-ph]].
- [25] L. Lopez Honorez and C. E. Yaguna, JCAP **1101** (2011) 002 [arXiv:1011.1411 [hep-ph]].
- [26] L. Lopez Honorez, E. Nezri, J. F. Oliver and M. H. G. Tytgat, JCAP **0702**, 028 (2007) [hep-ph/0612275]; T. Hambye and M. H. G. Tytgat, Phys. Lett. B **659**, 651 (2008) [arXiv:0707.0633 [hep-ph]]; P. Agrawal, E. M. Dolle and C. A. Krenke, Phys. Rev. D **79**, 015015 (2009) [arXiv:0811.1798 [hep-ph]]; T. Hambye, F. -S. Ling, L. Lopez Honorez and J. Rocher, JHEP **0907**, 090 (2009) [Erratum-ibid. **1005**, 066 (2010)] [arXiv:0903.4010 [hep-ph]]; E. Nezri, M. H. G. Tytgat and G. Vertongen, JCAP **0904**, 014 (2009) [arXiv:0901.2556 [hep-ph]]; S. Andreas, M. H. G. Tytgat and Q. Swillens, JCAP **0904**, 004 (2009) [arXiv:0901.1750 [hep-ph]]; C. Arina, F. -S. Ling and M. H. G. Tytgat, JCAP **0910**, 018 (2009) [arXiv:0907.0430 [hep-ph]]; L. Lopez Honorez and C. E. Yaguna, JHEP **1009**, 046 (2010) [arXiv:1003.3125 [hep-ph]]; A. Melfo, M. Nemevsek, F. Nesti, G. Senjanovic and Y. Zhang, Phys. Rev. D **84**, 034009 (2011) [arXiv:1105.4611 [hep-ph]]; M. Krawczyk, D. Sokolowska, P. Swaczyna and B. Swiezewska, JHEP **1309**, 055 (2013) [arXiv:1305.6266 [hep-ph]]; M. Gustafsson, S. Rydbeck, L. Lopez-Honorez and E. Lundstrom, Phys. Rev. D **86**, 075019 (2012) [arXiv:1206.6316 [hep-ph]]; E. M. Dolle and S. Su, Phys. Rev. D **80**, 055012 (2009) [arXiv:0906.1609 [hep-ph]]; S. Kanemura, Y. Okada, H. Taniguchi and K. Tsumura, Phys. Lett. B **704**, 303 (2011) [arXiv:1108.3297 [hep-ph]].
- [27] A. Arhrib, R. Benbrik and N. Gaur, Phys. Rev. D **85**, 095021 (2012) [arXiv:1201.2644 [hep-ph]].
- [28] B. Swiezewska and M. Krawczyk, Phys. Rev. D **88**, 035019 (2013) [arXiv:1212.4100 [hep-ph]]; arXiv:1305.7356 [hep-ph].

- [29] Q. -H. Cao, E. Ma and G. Rajasekaran, Phys. Rev. D **76**, 095011 (2007) [arXiv:0708.2939 [hep-ph]].
- [30] E. Dolle, X. Miao, S. Su and B. Thomas, Phys. Rev. D **81**, 035003 (2010) [arXiv:0909.3094 [hep-ph]]; X. Miao, S. Su and B. Thomas, Phys. Rev. D **82**, 035009 (2010) [arXiv:1005.0090 [hep-ph]].
- [31] E. Lundstrom, M. Gustafsson and J. Edsjo, Phys. Rev. D **79**, 035013 (2009) [arXiv:0810.3924 [hep-ph]].
- [32] R. Barbieri, L. J. Hall and V. S. Rychkov, Phys. Rev. D **74**, 015007 (2006) [hep-ph/0603188].
- [33] P. A. R. Ade *et al.* [Planck Collaboration], arXiv:1303.5076 [astro-ph.CO].
- [34] D. S. Akerib *et al.* [LUX Collaboration], arXiv:1310.8214 [astro-ph.CO].
- [35] M. Ackermann *et al.* [Fermi-LAT Collaboration], Phys. Rev. Lett. **107**, 241302 (2011) [arXiv:1108.3546 [astro-ph.HE]].
- [36] X. Huang, Q. Yuan, P. -F. Yin, X. -J. Bi and X. Chen, JCAP **1211**, 048 (2012) [Erratum-ibid. **1305**, E02 (2013)] [arXiv:1208.0267 [astro-ph.HE]].
- [37] M. Aguilar *et al.* [AMS Collaboration], Phys. Rev. Lett. **110**, 141102 (2013).
- [38] O. Adriani *et al.* [PAMELA Collaboration], Nature **458**, 607 (2009) [arXiv:0810.4995 [astro-ph]].
- [39] M. Ackermann *et al.* [Fermi LAT Collaboration], Phys. Rev. Lett. **108**, 011103 (2012) [arXiv:1109.0521 [astro-ph.HE]].
- [40] M. Ackermann *et al.* [Fermi LAT Collaboration], Phys. Rev. D **82**, 092004 (2010) [arXiv:1008.3999 [astro-ph.HE]].
- [41] O. Adriani *et al.* [PAMELA Collaboration], Phys. Rev. Lett. **105**, 121101 (2010) [arXiv:1007.0821 [astro-ph.HE]].
- [42] E. Aprile *et al.* [XENON100 Collaboration], Phys. Rev. Lett. **109**, 181301 (2012) [arXiv:1207.5988 [astro-ph.CO]].
- [43] M. Gustafsson, E. Lundstrom, L. Bergstrom and J. Edsjo, Phys. Rev. Lett. **99**, 041301 (2007) [astro-ph/0703512 [ASTRO-PH]].
- [44] M. E. Peskin and T. Takeuchi, Phys. Rev. D **46** (1992) 381.
- [45] M. Baak, M. Goebel, J. Haller, A. Hoecker, D. Kennedy, R. Kogler, K. Moenig and M. Schott *et al.*, Eur. Phys. J. C **72**, 2205 (2012) [arXiv:1209.2716 [hep-ph]].
- [46] K. Nakamura *et al.* [Particle Data Group Collaboration], J. Phys. G G **37**, 075021 (2010).

- [47] A. Pierce and J. Thaler, JHEP **0708**, 026 (2007) [hep-ph/0703056 [HEP-PH]].
- [48] M. Acciarri *et al.* [L3 Collaboration], Phys. Lett. B **472**, 420 (2000) [hep-ex/9910007];
R. Barate *et al.* [ALEPH Collaboration], Phys. Lett. B **499**, 67 (2001) [hep-ex/0011047];
J. Abdallah *et al.* [DELPHI Collaboration], Eur. Phys. J. C **31**, 421 (2003) [hep-ex/0311019];
G. Abbiendi *et al.* [OPAL Collaboration], Eur. Phys. J. C **35**, 1 (2004) [hep-ex/0401026].
- [49] ATLAS Collaboration, ATLAS-CONF-2013-011.
- [50] CMS Collaboration, CMS-PAS-HIG-13-018.
- [51] CMS Collaboration, CMS-PAS-HIG-13-013.
- [52] ATLAS Collaboration, ATLAS-CONF-2013-012.
- [53] C. Palmer [CMS Collaboration], arXiv:1305.3654 [hep-ex]; S. Chatrchyan *et al.* [CMS Collaboration], CMS-PAS-HIG-13-001.
- [54] CMS Collaboration, CMS-PAS-EXO-12-048.
- [55] ATLAS Collaboration, ATLAS-CONF-2012-147.
- [56] G. Belanger, F. Boudjema, A. Pukhov and A. Semenov, Comput. Phys. Commun. **180**, 747 (2009) [arXiv:0803.2360 [hep-ph]]; G. Belanger, F. Boudjema, A. Pukhov and A. Semenov, Nuovo Cim. C **033N2**, 111 (2010) [arXiv:1005.4133 [hep-ph]].
- [57] D. Larson, J. Dunkley, G. Hinshaw, E. Komatsu, M. R.olta, C. L. Bennett, B. Gold and M. Halpern *et al.*, Astrophys. J. Suppl. **192**, 16 (2011) [arXiv:1001.4635 [astro-ph.CO]].
- [58] K. Griest and D. Seckel, Phys. Rev. D **43**, 3191 (1991).
- [59] P. Binetruy, G. Girardi and P. Salati, Nucl. Phys. B **237**, 285 (1984).
- [60] A. Geringer-Sameth and S. M. Koushiappas, Phys. Rev. Lett. **107**, 241303 (2011) [arXiv:1108.2914 [astro-ph.CO]].
- [61] Y. -L. S. Tsai, Q. Yuan and X. Huang, JCAP **1303**, 018 (2013) [arXiv:1212.3990 [astro-ph.HE]].
- [62] Fermi-LAT Collaboration, Astrophys. J. Suppl. **199**, 31 (2012) [arXiv:1108.1435 [astro-ph.HE]].
- [63] J. Chang, J. H. Adams, H. S. Ahn, G. L. Bashindzhagyan, M. Christl, O. Ganel, T. G. Guzik and J. Isbert *et al.*, Nature **456**, 362 (2008).
- [64] F. Aharonian *et al.* [H.E.S.S. Collaboration], Phys. Rev. Lett. **101**, 261104 (2008) [arXiv:0811.3894 [astro-ph]]; F. Aharonian *et al.* [H.E.S.S. Collaboration], Astron. Astrophys. **508**, 561 (2009) [arXiv:0905.0105 [astro-ph.HE]].

- [65] D. Borla Tridon *et al.* [MAGIC Collaboration], arXiv:1110.4008 [astro-ph.HE].
- [66] O. Adriani *et al.* [PAMELA Collaboration], Phys. Rev. Lett. **106**, 201101 (2011) [arXiv:1103.2880 [astro-ph.HE]].
- [67] X. -G. He, Mod. Phys. Lett. A **24**, 2139 (2009) [arXiv:0908.2908 [hep-ph]]; Y. -Z. Fan, B. Zhang and J. Chang, Int. J. Mod. Phys. D **19**, 2011 (2010) [arXiv:1008.4646 [astro-ph.HE]]; P. D. Serpico, Astropart. Phys. **39-40**, 2 (2012) [arXiv:1108.4827 [astro-ph.HE]]; M. Cirelli, Pramana **79**, 1021 (2012) [arXiv:1202.1454 [hep-ph]].
- [68] G. Bertone, M. Cirelli, A. Strumia and M. Taoso, JCAP **0903**, 009 (2009) [arXiv:0811.3744 [astro-ph]]; L. Bergstrom, G. Bertone, T. Bringmann, J. Edsjo and M. Taoso, Phys. Rev. D **79**, 081303 (2009) [arXiv:0812.3895 [astro-ph]]; M. Cirelli, P. Panci and P. D. Serpico, Nucl. Phys. B **840**, 284 (2010) [arXiv:0912.0663 [astro-ph.CO]]; M. Papucci and A. Strumia, JCAP **1003**, 014 (2010) [arXiv:0912.0742 [hep-ph]].
- [69] D. Grasso *et al.* [FERMI-LAT Collaboration], Astropart. Phys. **32**, 140 (2009) [arXiv:0905.0636 [astro-ph.HE]]; T. Linden and S. Profumo, Astrophys. J. **772**, 18 (2013) [arXiv:1304.1791 [astro-ph.HE]]; P. -F. Yin, Z. -H. Yu, Q. Yuan and X. -J. Bi, Phys. Rev. D **88**, 023001 (2013) [arXiv:1304.4128 [astro-ph.HE]].
- [70] L. Bergstrom, T. Bringmann, I. Cholis, D. Hooper and C. Weniger, Phys. Rev. Lett. **111**, 171101 (2013) [arXiv:1306.3983 [astro-ph.HE]].
- [71] Q. Yuan, X. -J. Bi, G. -M. Chen, Y. -Q. Guo, S. -J. Lin and X. Zhang, arXiv:1304.1482 [astro-ph.HE]; Q. Yuan and X. -J. Bi, Phys. Lett. B **727**, 1 (2013) [arXiv:1304.2687 [astro-ph.HE]].
- [72] L. J. Gleeson and W. I. Axford, Astrophys. J. **154**, 1011 (1968).
- [73] O. Adriani *et al.* [PAMELA Collaboration], Science **332**, 69 (2011) [arXiv:1103.4055 [astro-ph.HE]].
- [74] A. De Simone, A. Riotto and W. Xue, JCAP **1305**, 003 (2013) [arXiv:1304.1336 [hep-ph]]; H. -B. Jin, Y. -L. Wu and Y. -F. Zhou, JCAP **1311**, 026 (2013) [arXiv:1304.1997 [hep-ph]].
- [75] O. Adriani, G. C. Barbarino, G. A. Bazilevskaya, R. Bellotti, M. Boezio, E. A. Bogomolov, L. Bonechi and M. Bongi *et al.*, Phys. Rev. Lett. **102**, 051101 (2009) [arXiv:0810.4994 [astro-ph]].
- [76] F. Donato, D. Maurin, P. Brun, T. Delahaye and P. Salati, Phys. Rev. Lett. **102**, 071301 (2009) [arXiv:0810.5292 [astro-ph]]; I. Cholis, JCAP **1109**, 007 (2011) [arXiv:1007.1160 [astro-ph.HE]].

- [77] M. Aguilar *et al.* [AMS Collaboration], Phys. Rept. **366**, 331 (2002) [Erratum-ibid. **380**, 97 (2003)].
- [78] Y. Asaoka, Y. Shikaze, K. Abe, K. Anraku, M. Fujikawa, H. Fuke, M. Imori and S. Haino *et al.*, Phys. Rev. Lett. **88**, 051101 (2002) [astro-ph/0109007].
- [79] Haino *et al.*, Proc. 29th Int. Cosmic Ray Conf. 3, 13 (2005).
- [80] R. R. de Austri, R. Trotta and L. Roszkowski, JHEP **0605**, 002 (2006) [hep-ph/0602028].
- [81] L. Roszkowski, E. M. Sessolo and Y. -L. S. Tsai, Phys. Rev. D **86**, 095005 (2012) [arXiv:1202.1503 [hep-ph]].
- [82] J. Alwall, M. Herquet, F. Maltoni, O. Mattelaer and T. Stelzer, JHEP **1106**, 128 (2011) [arXiv:1106.0522 [hep-ph]].
- [83] D. Hooper and L. Goodenough, Phys. Lett. B **697**, 412 (2011) [arXiv:1010.2752 [hep-ph]]; A. Boyarsky, D. Malyshev and O. Ruchayskiy, Phys. Lett. B **705**, 165 (2011) [arXiv:1012.5839 [hep-ph]]; D. Hooper and T. Linden, Phys. Rev. D **84**, 123005 (2011) [arXiv:1110.0006 [astro-ph.HE]]; K. N. Abazajian and M. Kaplinghat, Phys. Rev. D **86**, 083511 (2012) [arXiv:1207.6047 [astro-ph.HE]]; C. Gordon and O. MacÃas, arXiv:1306.5725 [astro-ph.HE].
- [84] J. Stahov, H. Clement and G. J. Wagner, Phys. Lett. B **726**, 685 (2013) [arXiv:1211.1148 [nucl-th]].
- [85] F. Feroz, M. P. Hobson and M. Bridges, Mon. Not. Roy. Astron. Soc. **398**, 1601 (2009) [arXiv:0809.3437 [astro-ph]].
- [86] W. A. Rolke, A. M. Lopez and J. Conrad, Nucl. Instrum. Meth. A **551**, 493 (2005) [physics/0403059].
- [87] S. Kanemura, S. Matsumoto, T. Nabeshima and N. Okada, Phys. Rev. D **82**, 055026 (2010) [arXiv:1005.5651 [hep-ph]].
- [88] A. Djouadi, A. Falkowski, Y. Mambrini and J. Quevillon, Eur. Phys. J. C **73**, 2455 (2013) [arXiv:1205.3169 [hep-ph]].
- [89] M. Klasen, C. E. Yaguna and J. D. Ruiz-Alvarez, Phys. Rev. D **87** (2013) 075025 [arXiv:1302.1657 [hep-ph]].
- [90] M. Pato, D. Hooper and M. Simet, JCAP **1006**, 022 (2010) [arXiv:1002.3341 [astro-ph.HE]].
- [91] A. Malinlin, <http://www.atlc.umd.edu/pub/ams/pub07/Malinin.LomonosovConf07.pdf>
- [92] C. Garcia-Cely and A. Ibarra, JCAP **1309**, 025 (2013) [arXiv:1306.4681 [hep-ph]].
- [93] G. L. Bayatian *et al.* [CMS Collaboration], J. Phys. G **34**, 995 (2007).